Theor Chem Acc (1999) 102:328–345
DOI 10.1007/s00214980m100

Theoretical
Chemistry Accounts

Regular article

Symmetry and broken symmetries in molecular orbital descriptions of unstable molecules II. Alignment, flustration and tunneling of spins in mesoscopic molecular magnets*

K. Yamaguchi, S. Yamanaka, M. Nishino, Y. Takano, Y. Kitagawa, H. Nagao, Y. Yoshioka

Department of Chemistry, Graduate School of Science, Osaka University, Toyonaka Osaka 560-0043, Japan

Received: 5 August 1998 / Accepted: 9 September 1998 / Published online: 17 December 1998

Abstract. As an extention of previous work [Yamaguchi K (1983) *J Mol Structure* (*Theochem*) 103:101], our theoretical efforts toward molecular materials are briefly reviewed. Axial, helical and general (cone, tetrahedron, etc) spin structures of carbon clusters, manganese oxide clusters and iron-sulfur clusters were investigated using the classical Heisenberg model and generalized Hartree-Fock theory. The spin flustrations in the clusters were also studied in relation to theoretical descriptions of the magnetism and the chemical bonds in active sites of several enzymes. The macroscopic quantum tunneling and coherence of spins in the manganese oxide clusters were analyzed using the instanton model, and the tunneling rate of spins was calculated by the coherent state path integral method. The spin transitions induced by an external magnetic field were studied by the path integral Monte Carlo method. The theoretical results were explained in terms of the symmetry and broken symmetry of the wavefunctions in the mesoscopic molecular systems, which are intermediate in the scale factor. The results were also applied to molecular design of mesoscopic clusters of clusters in the intermediate and strong correlation regime. The active control of spins is finally discussed from the viewpoint of functionalities in molecular and biological materials, and technological applications of mesoscopic molecular magnets are discussed with regard to quantum computing.

Key words: Symmetry and broken symmetry – Spin fluctuation – Spin tunneling – Spin alignment – Mesoscopic molecular magnets

1 Introduction

In a previous publication dedicated to Professor Fukui [1] we discussed the instabilities and broken symmetries in molecular orbital (MO) descriptions of unstable chemical bonds. Such concepts were introduced for theoretical understanding of irregular chemical reactions [2]. For example, the instability of chemical bonds was extensively studied in relation to nonconcerted behavior observed in various gas-phase reactions of unstable species such as carbenes, nitrenes, oxygen atoms, and multi-center biradicals. The orbital symmetry control for 1,3-dipolar reactions was often lost because of significant biradical character of 1,3-dipolar species such as oxygenated dipole, though the reactions are formally symmetry-allowed [1, 3]. The orbital symmetry breakings and electron localizations are also recognized for many binuclear metal complexes [4], organometallic conjugated systems [5], metal clusters and amorphous materials [6], which often exhibit high catalytic activity. The instability and symmetry-breaking of molecular orbitals would be important in several biological systems, where strained states of active sites are stabilized by proteins. As an example, a model of cytochrome *c* oxidase was recently examined by the broken-symmetry density functional theory (DFT) method [7].

Instabilities and broken symmetries in condensed matter physics have been discussed in relation to various interesting phenomena such as ferro- and antiferromagnetism, superconductivity and superfluidity, etc [8]. These are closely related to the phase transitions of metal complexes, organometallic compounds and organic materials. In past decades, intersection areas between quantum chemistry and condensed matter physics have deen developing because of the discovery and synthesis of many molecule-based materials such as organic metals, organic superconductors and organic ferromagnets. Recently quantum dynamics of spins has been investigated in relation to macroscopic quantum tunneling (MQT) and macroscopic quantum coherence (MQC) in mesoscopic molecular magnets [9].

In past decades we were interested in molecular materials based on active control of spins in organic radicals, ion-radicals generated by doping, transition metal ions, etc. For example, general spin structures of organic radicals were first discussed by spin vector models using

* Contribution to the Kenichi Fukui Memorial Issue

Correspondence to: K. Yamaguchi

the classical Heisenberg model for cyclic radical systems [10]. The spin correlation functions obtained by the generalized Hartree–Fock (GHF) solution were also discussed in relation to spin alignments in cyclic organic radicals [11]. Spin polarization and spin delocalization rules were applied to design ferro- and ferri-magnetic organic crystals and polymers, organic ferromagnetic metals, organometallic magnetic systems, etc [12]. The mean-field theory combined with the calculated effective exchange integrals was successfully utilized to estimate the temperatures of ferro- and antiferro-magnetic phase transitions of *p*-nitrophenyl nitronylnitroxide crystals. Recently, possibilities of spin-mediated superconductors and photo-induced superconductors were also examined theoretically [14]. Here, we briefly summarize our recent efforts toward molecular materials belonging to the intersection areas between quantum chemistry and solid-state physics.

This paper is organized as follows. In Sect. 2, we summarize briefly the theoretical background. In Sect. 3, we introduce ab initio calculations of the effective exchange integrals in the Heisenberg model. Then we discuss spin flustrations and spin tunneling in Sects. 4 and 5, respectively. We conclude with our interests for the future in the field of molecular materials in Sect. 6.

2 Theoretical background

2.1 Symmetry

Symmetry operations play important roles for characterization of various phenomena in material science. The spin-free Hamiltonians commute with the symmetry elements of time-reversal (T), spin-rotation (S_R), point group (P_N) and permutation (S_N) group [15]. Hence, these four symmetry operations are useful for consideration of the relations between solutions of several model Hamiltonians. The quantum Heisenberg Hamiltonian involves only the spin variable. Therefore, it can be completely characterized by the S_N group. Since, in the case of spin clusters, various valence-bond (VB) structures belong to irreducible representations of the S_N group, the spin couplings between the components can be expressed in terms of the S_N group [16]. The classical Heisenberg model, on the other hand, treats spin moments whose mutual directions are utilized to express spin structures in the clusters. The magnetic point group M_N will be useful for their characterization: $M_N = H_N + T(P_N - H_N)$, where H_N is a subgroup of P_N [17].

The GHF solution is given by general spin orbitals (GSO), which are characterized by three different symmetry operations: T, S_R and P_N.

$$\phi_i = \varphi_i^+ \alpha + \varphi_i^- \beta \tag{1}$$

Therefore, any orbital set belongs to the irreducible representation of a subgroup of the direct product group, $T \times S_R \times P_N$ [18]. In most cases, the ground GHF spin orbitals have the full symmetry of the direct group. Thus in GHF theory, spin alignments can be characterized by both spin ($T \times S_R$) and space (P_N) symmetries. An extended HF wavefunction can be constructed by use of the direct product group $G = S_N \times T \times S_R \times P_N$ [19]. The group-theoretical relationships between solutions of various model Hamiltonians were already shown in the cases of iron-sulfur clusters involved in ferredoxins [20] and vanadium-oxide clusters [21]. The phase symmetry (ϕ) should be considered for the Hartree–Bogoliubov solution responsible for superconductivity [22]. The number density projection is necessary for the solution to recover the broken symmetry of the particle number, N, in finite systems [19].

2.2 Correlation corrections

MO calculations are feasible for relatively large clusters even at the ab initio level. We first obtain stable HF and/or Hartree–Bogoliubov or density functional solutions for clusters under investigation. The model (active) space is constructed from occupation number and natural orbitals (NO) of these solutions [23]; for example unrestricted Hartree–Fock (UHF) NO (UNO), GHF NO, DFT NO. In order to obtain dynamical correlation corrections, these NO are utilized for basis functions (kets) of proper computational methods, which are CI, many-body perturbation [24], coupled cluster (CC) [23] and path integral Monte Calro (PIMC) [25] procedures. For example, UNO CASCI, UNO CASSCF and UNO CASPT2 methods were applied to elucidate an impor-

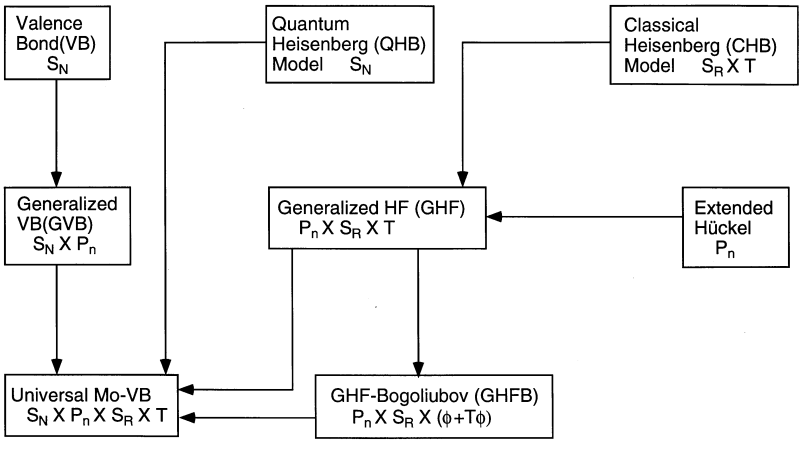

Fig. 1. Various models, symmetry operations (T, S_R, S, S_N) and the interrelationships among the models on the basis of group theory

tant role of electron correlation for effective exchange interactions between open-shell species [26]. The UNO PIMC method was useful for ab initio quantum simulation of spins under an external magnetic field at a finite temperature [27]. The details of these computational techniques are given in Refs. [25, 27]. In this paper, we briefly summarize key aspects relating to spin alignments in the following section.

2.3 Spin structure and Heisenberg model

Notations of spin structures are briefly explained by using three- and four-centered systems [21]. Figure 2 illustrates schematically helical and torsional spin structures, which have 2D and 3D spin components, respectively. The HF solution with the 1D spin structure is called the axial spin density wave (ASDW), which is equivalent to the UHF solution in quantum chemistry. The HF solutions with the 2D and 3D spin structures are denoted as the helical SDW and the torsional SDW, respectively [18].

Before the construction of GHF solutions, the classical Heisenberg model provides possible spin alignments characterized by the magnetic group $(T \times S)$ [21, 28].

$$H = -\sum 2 J_{ab} S_a S_b \cos\theta_{ab} \tag{2}$$

where θ_{ab} means the angle between spin vectors as shown in Fig. 2 and S_c $(c = a, b)$ is the magnitude of spin. Since spin alignments often have magnetic symmetries, spin alignment rules are described in terms of the magnetic group. The magnetic group notations of triangular and cone-type spin alignments in Fig. 2 are given in our previous papers [10, 15, 19].

The effective exchange integrals (J_{ab}) in Eq. (2) have been experimentally determined by measurement of the magnetic susceptibility. On the other hand, it can be calculated by the combination of the GHF solution with the Heisenberg model. The GHF solution is generally given by a Slater determinant consisting of GSO in Eq. (1)

$$\Phi = |\phi_1 \phi_{2\ldots\ldots} \phi_{i\ldots\ldots} \phi_n| \ . \tag{3}$$

Since the GHF solution involves many spin components characterized by $\mathbf{S}^2$ and $\mathbf{S}_z$ operators, it can be expanded by spin-adapted wavefunctions [19] as

$$\Phi = \sum C(S, M_z)]\Phi(S, M_z) \ , \tag{4}$$

where $C(S, M_z)$ denotes a fraction of the wavefunction with the S and M_z eigenvalues.

Assuming energy splittings obtained by the Heisenberg model for spin states (S) in Eq. (4), we can have the following simple relation on the basis of the spin-projection procedure [4]

$$J_{ab} = [{}^{\mathrm{LS}}E(\mathrm{GHF\text{-}X}) - {}^{\mathrm{HS}}E(\mathrm{UHF\text{-}X})]/ \\ [{}^{\mathrm{HS}}\langle \mathbf{S}^2(\mathrm{UHF\text{-}X})\rangle - {}^{\mathrm{LS}}\langle \mathbf{S}^2(\mathrm{GHF\text{-}X})\rangle] \tag{5}$$

where LS and HS mean the lowest spin and highest spin states, respectively, and ${}^{Z}E(\mathrm{Y})$ and ${}^{Z}\langle \mathbf{S}^2(\mathrm{Y})\rangle$ denote, respectively, total energy and total spin angular momentum of the spin state Z by the solution Y. X in Eq. (5) means Møller-Plesset (MP) perturbation and CC methods as post GHF(UHF) approximations to include dynamical correlation effects [29]. Since the GHF solution often reduces to UHF(ASDW) in the LS state for the case of 1D spin structure, the J_{ab} value can be calculated within the UHF approximation as illustrated in Fig. 3A. The spin-polarized density functional methods are also efficient in this situation [30]. On the other hand, the GHF solution is necessary for the LS state in more general cases such as 2D and/or 3D spin structures, as shown in Fig. 3B.

3 Ab intio calculations of J_{ab} values

3.1 Superexchange interactions

In this section, we consider superexchange interactions [31] in several isoelectronic species shown in Fig. 4. The sulfur ylides and/or oxygenated dipoles (**1**) with planar conformations are well-known 1,3-dipolar compounds with a singlet ground state [3]. The reactivity of these species was investigated in an earlier paper [1]. Here, we consider their electronic structures from the viewpoint of superexchange interaction in molecular magnetism. The direct exchange interaction between the terminal π radicals in the biradical structure (**2**) is rather weak because of the long distance as shown in Fig. 4, leading to quasi-degeneracy between singlet and triplet configurations. However, electron transfer from the sulfur (or oxygen) atom to the left or right radical orbital is feasible to provide zwitterionic structures **3** and **4**. The singlet state is therefore described by the superposition of these three configurations [3]. This configuration-mixing stabilizes the singlet state: the strong π bond between the cation radical of the central hetero atom and the terminal radical is formed in the case of a zwitterion because of the strong $p\pi$-$p\pi$ overlap. The

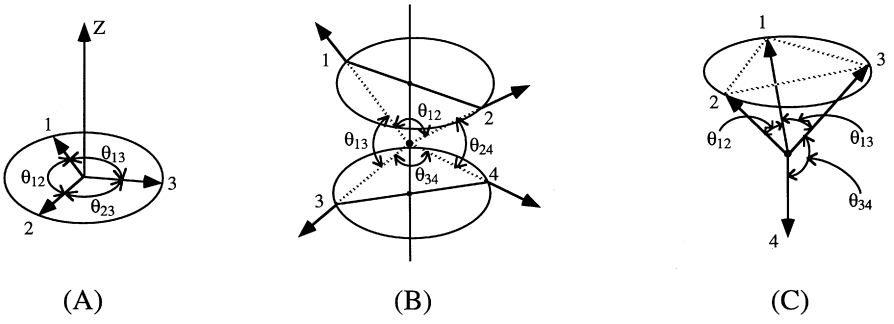

Fig. 2A–C. Coordinate axes for helical and torsional spin structures. **A** illustrates a helical spin structure for three spin systems. **B** and **C** depict spin structures with the cone- and top-type symmetries, respectively

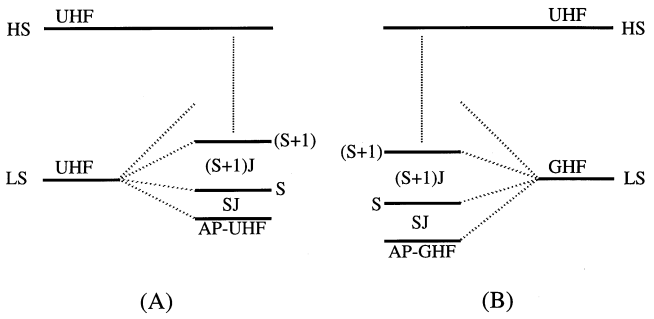

Fig. 3A, B. Approximate spin projection (*AP*) schemes for unrestricted Hartree–Fock (*UHF*) and generalised Hartree–Fock (*GHF*) solutions. Energy levels for AP-UHF and AP-GHF are illustrated by using the size of spin (S) and the effective exchange integral (J) in **A** for 1D spin structure and in **B** for 2D and 3D spin structures, respectively

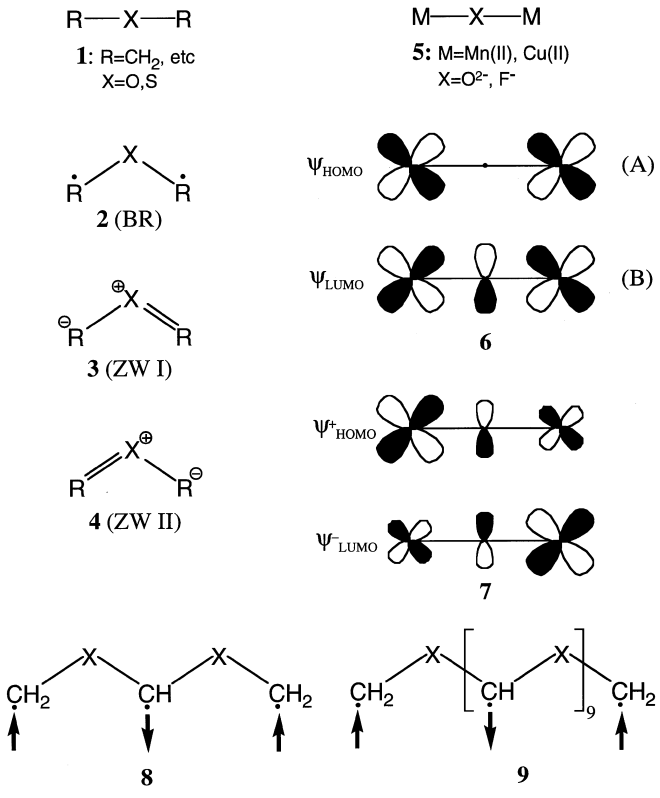

Fig. 4. Structures of sulfur ylides and/or oxygenated dipole (1) and transition metal oxides (**5**). A biradical structure and zwitterionic structures are expressed by **2**, **3** and **4**, respectively. **6** illustrates the symmetry-adapted $d\pi$-$p\pi$-$d\pi$ HOMO and LUMO. The broken symmetry MOs described by the different-orbitals-for-different-spins are shown in **7**. **8** and **9** denote the trimer and olygomer with the eleven magnetic sites, respectively

stabilization of the low-spin state by this interaction is often called the superexchange mechanism [31].

The heroatoms in **1** can be used as antiferromagnetic couplers in organic magnetic olygomers and polymers. Such possibilities are discussed in detail in Sect. 6. The transition metal oxides (MOM) (M = Cu(II), Ni(II), Fe(III), etc) (**5**) examined previously [4] also have low-spin ground states. In fact, these species have $d\pi$-$p\pi$-$d\pi$ type HOMOs and LUMOs as illustrated by **6** in Fig. 4, though these MOs are actually symmetry-broken because of the strong electron correlation as described by the different-orbitals-for-different-spins as shown by **7** in Fig. 4 [31].

$$\psi^{\pm}_{\mathrm{HOMO}} = \cos\theta\psi_{\mathrm{HOMO}} \pm \sin\theta\psi_{\mathrm{LUMO}} \tag{6}$$

Other d—p conjugated bonds for MOM are more or less localized, and the Heisenberg model can be applied to describe effective exchange interactions between magnetic ions.

We performed ab initio UHF calculations of MOM by using the Takewaki-Huzinaga MINI basis set [32] to estimate J_{ab} values in Eq. (5) [4]. Here, their MIDI plus Hay's diffuse d-basis sets, [533(21)/53(21)/(411)] for transition metal ions and MIDI plus diffuse sp orbitals for anion parts, were employed for re-examination of previous results. As an example, let us consider the linear Mn(II)OMn(II) (**5a**) dimer where $S = 5/2$ for Mn(II). In this case, the J_{ab} value is given by the orbital-averaged value, $J_{ab} = \sum J_{ij}/25$. The potential curve and J_{ab} values obtained by the above method are shown in Fig. 5. From Fig. 5, the optimized Mn—O distance is about 1.84 Å, and the J_{ab} value at this distance is about $-4\ \mathrm{cm}^{-1}$. However, the sign of J_{ab} changes at $R = 1.9$ Å; it becomes positive (ferromagnetic) in a R region further than 1.9 Å. Thus the spin crossover occurs in this system. On the other hand, the magnitude of the J_{ab} value increases sharply with decrease of the Mn—O distance as shown in Fig. 5, since antiferromagnetic interaction becomes strong because of the superexchange mechanism. Judging from the present result, the previous results [4] obtained for MOM using the MINI basis set are qualitatively correct.

3.2 Correlation corrections

The precursor of the high-temperature superconductor [33], La_2CuO_4 has an antiferromagnetic insulator constructed of the Cu(II)OCu(II) (**5b**) bond. This compound is isoelectronic to K_2CuF_3 and K_2NiF_4 crystals, which have the 2D antiferromagnetic sheet. We extracted the linear binuclear systems MXM [M = Cu(II), Ni(II) and Mn(II)] as the model clusters [34]. The effective exchange integrals for the binuclear systems were calculated using Eq. (5). To this end, UHF MP computations using the above-mentioned triple-zeta basis set were carried out. It was found that the calculated J_{ab} values at the optimized M-F distances are $-56, -12$ and $-1\ \mathrm{cm}^{-1}$, respectively, for Cu(II), Ni(II) and Mn(II) in the MFM^{3+} (**5c**) system. On the other hand, the corresponding values by approximately spin-projected (AP) UMP4 (2) methods were -134 (-111) and -22 (20) cm^{-1}. These values are consistent with the experimental values ($-132, -36$ and $-3\ \mathrm{cm}^{-1}$) for the Cu(II), Ni(II) and Mn(II) fluorides with the K_2NiF_4-type structure [35]. The correlation corrections are thus important for quantitative calculations of superexchange interactions between transition metal ions via a fluoride anion.

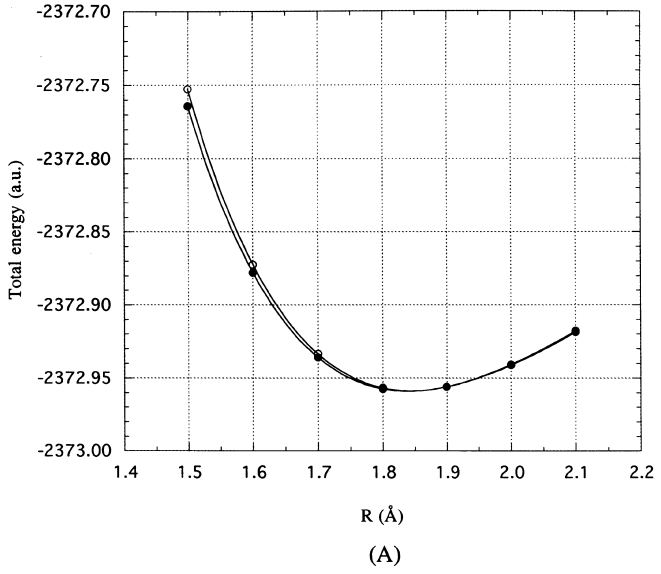

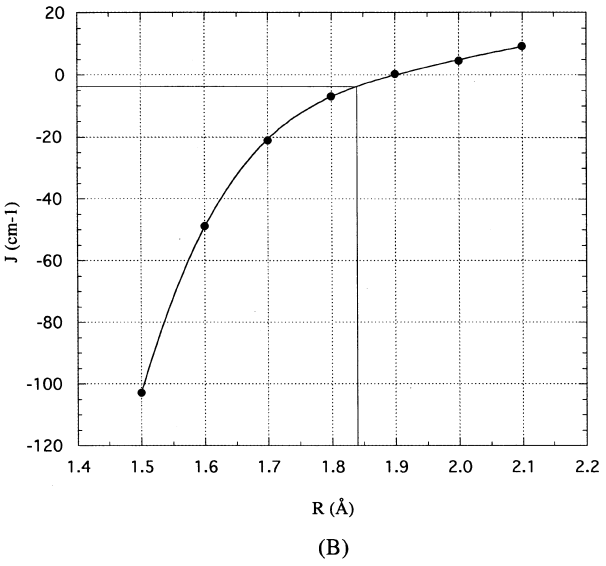

Fig. 5A. Variations of total energies for the low (•) and high (○) spin states and **B** variation of J_{ab} values of Mn(II)OMn(II) with Mn-O distance. The J_{ab} value at the optimized Mn-O distance is depicted

Here, APUMPn calculations were carried out for the Cu(II)OCu(II) (**5b**) unit, which is the simplest antiferromagnetic unit in La_2CuO_4. The potential curves and J_{ab} values by APUMPn methods are illustrated in Fig. 6. The J_{ab} values by APUHF and APUMP4(2) are, respectively, -250 and -800 cm^{-1} at the optimized Cu—O distance. The latter value is consistent with the experimental value (-1000 cm^{-1}) for the CuO chain in various cupurates [36]. The magnitudes of the calculated J_{ab} values for Mn(II) and Cu(II) oxides are quite different, and this tendency is parallel to the experiments for transition metal oxides. The present example clearly indicates an important role of dynamical correlation corrections for the UHF solution to obtain reasonable J_{ab} values for transition metal oxides.

3.3 Size-consistent spin projection

Recently many magnetic clusters have been synthesized, and ab initio computational methods are applied to the systems. For this purpose, it is noteworthy that the size-consistency condition should be retained after spin projection, since polyradical species of our present concern have over ten spin sites. Since total energies of the HS UHF and LS GHF solutions correspond to those of the Heisenberg models, respectively, the energy gap can be used to estimate effective exchange integrals (J_{ab}) for uniform linear chains in Fig. 4 [37] as

$$J_{ab}(\mathrm{Z}) = [{}^{\mathrm{LS}}E(\mathrm{Z}) - {}^{\mathrm{HS}}E(\mathrm{Z})]/D(\mathrm{ZI}) \ , \qquad (7)$$

where,

$$D(\mathrm{ZI}) = 4(N-1)S_aS_b \qquad (8)$$

and Z = GHF(UHF) or DFT and N is the number of spin sites in the clusters under consideration. S_a and S_b are sizes of spin at sites a and b. The energy gain by the spin projection can be estimated by Eqs. (7) and (8), since J_{ab}(Z) is determined even for larger systems. If the electron correlation is taken into account under the

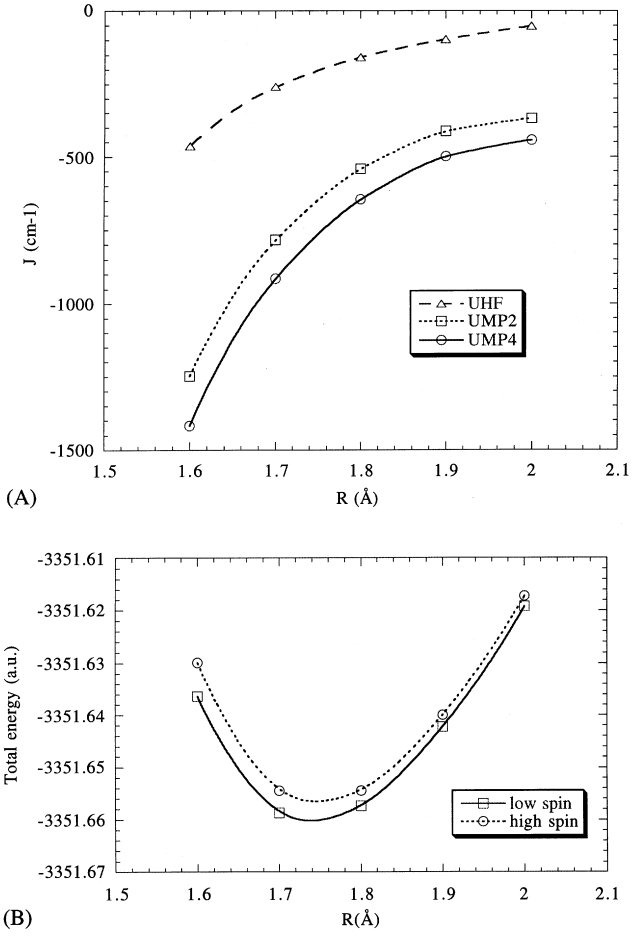

Fig. 6A. Variations of the calculated J_{ab} values by UHF, UMP2 and UMP4 and **B** variation of total energies for the low and high spin states of Cu(II)OCu(II) by UMP4 with Cu-O distance

GHF(UHF) approximation, the effective exchange integral by GHF(UHF) in Eq. (7) is replaced by that of GHF-X [X = MP, CCSD, CCSD(T)].

$$J_{ab}(\text{GHF-X}) = [{}^{\text{LS}}E(\text{GHF-X}) - {}^{\text{HS}}E(\text{UHF-X})]/D(\text{ZI}) \ . \tag{9}$$

On the other hand, the spin projection of the GHF-X wavefunctions in the intermediate correlation regime is a difficult task, since orbital overlaps between radical orbitals are significantly large. The Löwdin-type spin-projection scheme [38] is utilized for this purpose; however, it often provides wrong J_{ab} values because of the approximations introduced [38]. Alternately, approximate spin projections [3, 29, 30] are feasible for G(U)HF-based and spin-polarized DFT methods to calculate potential curves for dissociations from near closed-shell to the localized limit. To this end, we have considered an approximate but size-consistent spin-projection procedure, where the denominator in Eq. (7) is modified so as to reproduce the extreme values of the total spin angular momentum as [37]

$$D(\text{ZII}) = {}^{\text{HS}}\langle S^2\rangle(\text{Z}) - {}^{\text{LS}}\langle S^2\rangle(\text{Z}) - S_a g(N)[{}^{LS}\langle S^2\rangle(\text{Z}) - S_{\text{r}}(S_{\text{r}}+1)] \ , \tag{10}$$

where

$$g(N) = (N-2)2/N \quad (N > 2 \text{ and even numbers}), \quad \text{or} \tag{11a}$$

$$= (N-3) \quad (N > 3 \text{ and odd numbers}), \tag{11b}$$

and Z = UMP(GMP), UCC(GCC) or DFT, and S_{r} denotes the exact spin angular momentum for clusters under discussion.

$$S_{\text{r}} = n(S_a - S_b) \qquad (N = 2n), \text{ or} \tag{11c}$$

$$S_{\text{r}} = n(S_a - S_b) + S_a \qquad (N = 2n+1) \ . \tag{11d}$$

The effective exchange integral by the AP-UMP(GMP), AP-UCC(GCC) and AP-DFT methods is, therefore, given by

$$J(\text{AP-Z}) = [{}^{\text{LS}}E(\text{Z}) - {}^{\text{HS}}E(\text{Z})]/D(\text{ZII}) \ . \tag{12}$$

The J(AP-Z) value almost reduces to that of Eq. (7) in the strong magnetic region, while it becomes a theoretical parameter for spin projection in the intermediate and strong overlap regions, where spin contamination effects in UHF and spin-polarized DFT wavefunctions are more or less decreased.

3.4 Linear clusters of 1,3-biradicals

Earlier [1], we throughly examined the biradical character of 1,3-dipolar species [3]. Here, let us first consider dimers, trimers, and clusters ($N = 11$) of 1,3-dipolar species as illustrated in Fig. 4. The effective exchange interactions between methylene groups via the oxygen (**1b**) or the sulfur (**1c**) atom in the dimer were calculated from Eqs. (7) and (12) using total energies of the LS singlet and the HS triplet states of **1** by the UHF/6-31G* method. Table 1 summarizes the results calculated using the 6-31G* basis set. The calculated J_{ab} values were negative (antiferromagnetic) according to all the methods examined here. The magnitudes of J_{ab}(UHF) by Eq. (7) and J_{ab}(APUHF) by Eq. (12) are quite similar, showing that the orbital overlaps between the magnetic orbitals are small. However, the J_{ab}(APUHF) values are different from the corresponding J_{ab} values by UNO CASSCF, which utilizes two active orbitals and two active electrons $\{2,2\}$ [23, 29]. On the other hand, the AP-DFT method approximately reproduces the CASSCF results. The spin-projection effect is remarkable for DFT, indicating that the orbital overlap between magnetic orbitals is relatively large because of the superexchange mechanism. This in turn indicates that UHF underestimates the superexchange interaction, and therefore should be improved by the MP and CC corrections [29].

Table 1. Effective exchange integrals for oligomers of 1,3-dipolar species by unrestricted Hertree–Fock(*UHF*) and density functional theory methods

System		C—O—C		C—S—C	
		None	AP[a]	None	AP
Dimer	UHF	−160	−155	−915	−880
	UNO CASSCF{2,2}		−1172		−2188
	UB3LYP	−2719	−2135	−3144	−2455
	UBLYP	−4375	−2822	−4589	−2902
Trimer	UHF	−30	−30	−62	−61
	UB3LYP	−2094	−1738	−2157 (−3056)	−1814 (−2570)
	UBLYP	−3398	−2500	−3116 (−4414)	−2319 (−3285)
11 mer	UHF	66	63	−365	−372
	UB3LYP	−1576	−876	−1471	−867
	UBLYP	−2680	−1050	−2175	−905

[a] Approximate spin projection

Next, we examined the trimer (**8**) as illustrated in Fig. 4 to elucidate the effect of the next nearest J_{ac} value. The spin-projection effect is remakable for **8**. The J_{ab} value for **8** becomes smaller than the corresponding J_{ab} values for the dimer (**1**). This means that the next-nearest neighbour exchange integral (J_{ac}) should be taken into account for this species. In fact, the simple relation $J_{ab}(\text{trimer})/J_{ab}(\text{dimer}) = 12/17$ was derived if the J_{ac} value was included for the Heisenberg model. The scaled J_{ab} values for **8** are close to the J_{ab} values for **1** as shown in parentheses in Table 1.

The linear cluster (**9**) composed of 11 radical sites in Fig. 4 was examined by the UHF and DFT/6-31G* method. The total energies of both the LS doublet and HS 13th multiplet ($S = 11/2$) states of **9** were calculated. From Table 1, both J_{ab} values by UB3LYP and UBLYP are negative in sign, showing antiferromagnetic spin alignment. On the other hand, the UHF calculations predict the ferromagnetic exchange interaction, showing the necessity of the MP and CC corrections [29]. The scaling factor for the J_{ab} value ($N = 11$) is about 1/2 if the next-nearest J_{ac} value is included for modeling by the Heisenberg model. Therefore the scaled J_{ab} values are

similar in the clusters. The present numerical results conclude that the AP-DFT method is useful for practical computations of J_{ab} values for strongly exchange coupled magnetic clusters, though MP and CC calculations, or CASSCF plus CASPT2 calculations are desirable for large clusters [30]. In fact, DFT(BLYP) often overestimates the stability of low-spin states [30]. Modification of the hybrid method (B2LYP) is necessary to reproduce the UCC and/or CASPT2 results for small magnetic model compounds, and then the modified B2LYP (MB2LYP) can be applied to related large magnetic systems.

4 Spin flustration

4.1 Classical Heisenberg models

The Heisenberg model can be applied to multicenter polyradicals which are insulators from the viewpoint of conductivity [21]. We have considered only the nearest-neighbor effective exchange integrals: this approximation is reliable at least for qualitative purposes. The Heisenberg model was successfully applied to derive selection rules for radical reactions based on the VB concept [28]. On the other hand, the $\mathbf{S}_i \cdot \mathbf{S}_j$ term is nothing but the spin-correlation function in solid-state physics, and the arrow the notation ($\uparrow\downarrow$ or $\uparrow\uparrow$) is a classical vector representation of singlet or triplet spin correlation between spins at the ith and jth sites [11]. Then we have a classical version of the Heisenberg model given by Eq. (2). It was already applied to derive general spin structures of organic radicals [10]. Now it is applied to obtain pictorial understanding of spin flustration, which is of current interest in relation to spin-gap and spin-mediated superconductivity [14, 36].

The spin alignments for multicenter polyradicals are described by the spin-vector model, since the present purpose is limited to obtaining qualitative pictures of spin flustrations [36]. Let us consider the Heisenberg model for the three-sites three-spins $\{3,3\}$ system. We can imagine linear H_3 radicals and allyl radicals as typical examples of this $\{3,3\}$ group [10]. From Eq. (2), the ground spin structure is parallel (high-spin) and antiparallel (low-spin), respectively, depending on positive and negative J_{ab} values as illustrated in **10** and **11** in Fig. 7. The cyclization of this linear system to the triangular system entails variations of spin structures from **10** to **12** and from **11** to **13**. The triplet pair is formed between sites 1 and 3 even in the low-spin structure **13** for which $J_{13} < 0$. Other spin structures such as **13** are also allowed for the low-spin state, showing the so-called spin flustration among possible three structures.

The more general spin structure **15** is possible at the triangular conformation, for which the θ_{ij} value in Eq. (2) is 120° [10]. Penny's bond order ($\cos\theta_{ij}$) becomes $-1/2$ for **15**, showing that the singlet spin coupling becomes the maximum ($-3/2$): note that it is -1 for **13** and **14** because of spin frustration. It represents the spin structure for the transition state of exchange-forbidden free-radical reactions [11]. However, such helical spin alignments have not yet been realized in the case of molecule-based magnets.

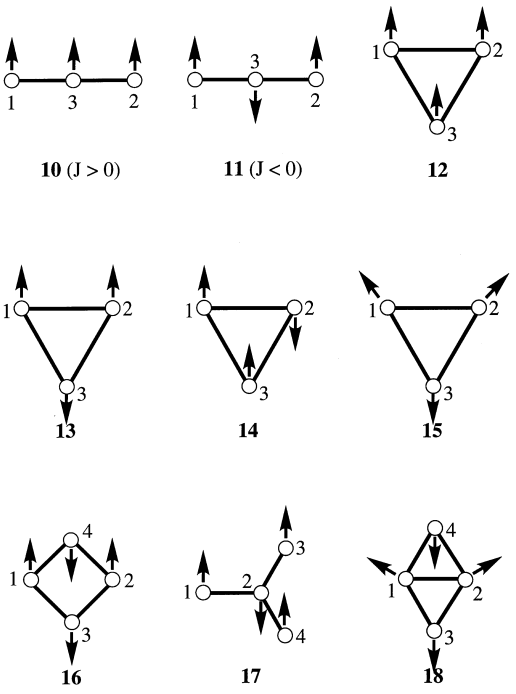

Fig. 7. Spin structures derived by the classical Heisenberg models for various spin systems. 10–15 illustrate spin structures for three-sites three-spins systems. Solutions for four-sites four-spins systems are shown in 16, 17 and 18

Next, let us consider the four-sites four-spins $\{4,4\}$ system. The H_4 radical and Cu_4O_4 core in cupric oxides with the D_{4h} conformation has a low-spin ground state with antiparallel spin alignment (**16**) because of negative J_{ab} values [21]. On the other hand, the high-spin, more exactly ferrimagnetic spin, structure (**17**) is predicted for the H_4 and many other $\{4,4\}$ systems with the D_{3h} conformation even though $J < 0$. The helical spin structure (**18**) is expected for a butterfly shape. As shown in Fig. 1, the corresponding GHF and universal MO-VB solutions for **15** and **18** can be constructed as described in Refs. [15, 21]. Here, we discuss only spin flustrations in hydrocarbon clusters and manganese oxide clusters within the spin-Hamiltonian models as shown below.

4.2 Applications to hydrocarbon polyradicals

Spin alignments (**10–18**) in Fig. 7 have been applied to predict ground spin states of simple hydrocarbon polyradicals. Some of them are depicted for explanation in Fig. 8. **11a** and **15a** represent the ground spin structures of allyl and cyclopropenyl radicals, respectively, since J_{ab} is negative because of the $p\pi$-$p\pi$ overlap. **16a** and **17a** describe the singlet and triplet ground states of cyclobutadiene and trimethylenemethane, respectively. **18a** corresponds to a helical spin structure for the diamond shape of the C_4 unit: it is noteworthy that no triplet site exists in this general spin alignment, though it appears at the 1,3-pair if axial structure is assumed. **19** and **20** show the high-spin and low-spin ground states of planar bis(methylene)cyclobutadiene. The rotation of

terminal radical group(s) is essential to induce the spin crossover from low-spin to high-spin in the case of **20**. **21** predicts the low-spin ground state of planar tetra(methylene)ethylene, showing that internal rotation around the central C—C bond is crucial for the high-spin ground state.

The local triplet site appears in the axial spin structure **22** for fulvene, while the general spin structure **23** involves only the singlet-type pair because of spin flustration. **23** is regarded as a coupled structure of methyl and cyclopentadienyl radicals; the latter has the pentagonal general spin structure. The general spin structure **24** is also predicted for heptafulvene, since cycloheptenyl radical has the D_{7h} general spin structure. Thus nonalternant hydrocarbones without bond alternations are expressed by combinations of general spin structures

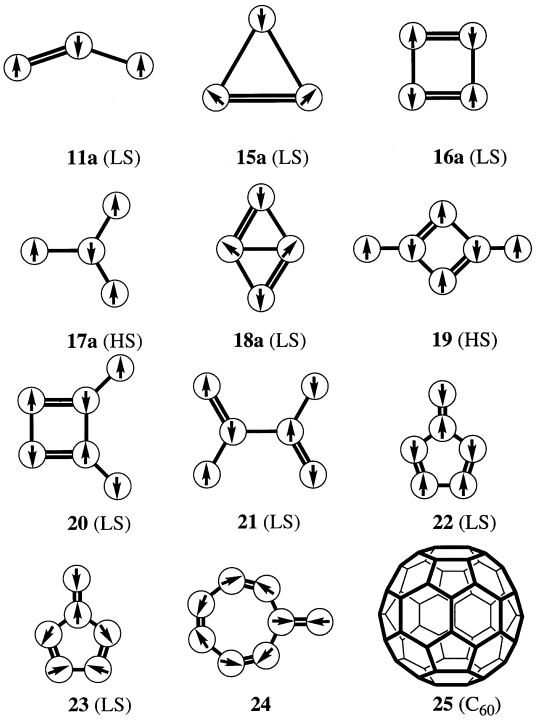

Fig. 8. Spin structures for hydrocarbon systems with linear, triangular, square planar, butterfly and other structures

(**15a**, **18a**, **23** and **24**) under the vector representation of spins. This implies that these species should exhibit paramagnetic susceptibilities because of the contribution of triplet-coupled singlet components ($\uparrow\uparrow\downarrow\downarrow$) involved in general spin structures. Bond alternations are therefore inevitable for the species to suppress such contributions, and tight singlet pairs are formed as illustrated in **22**, guaranteeing diamagnetic susceptibility. Thus, we must consider nonuniform Heisenberg chains for nonalternant hydrocarbons as

$$\hat{\mathrm{H}}_{NU} = -2\sum J_{i(i+1)}\mathbf{S}_i \cdot \mathbf{S}_{i+1} - 2\sum J_{i(i-1)}\mathbf{S}_i \cdot \mathbf{S}_{i-1} \quad (13)$$

where $|J_{i(i+1)}| \gg |J_{i(i-1)}|$. Since C_{60} involves the five-membered ring, it is described by a general spin structure constructed of superposition of the D_{5h} helical spin alignment if bond alternation is not considered. However, it actually occurs in C_{60} to provide olefinic double bonds as shown in **25** which are reactive to several reagents. Electron doping of C_{60} may entail such spin flustration since the bond alternation effect is relaxed [39].

4.3 Spin flustrations in manganese oxide clusters

Judging from the magnitude of spin density calculated for Mn(II)OMn(II), a spin S_i on a manganese ion could be regarded as a localized spin vector in order to obtain a simple expression of spin flustration; the magnitude of spin S_i in Eq. (2) is as follows, $S_i = 3/2$ for the Mn(IV) ion and $S_i = 2.0$ for the Mn(III) ion in manganese-oxygen clusters. It will be shown that the spin vector model is useful at least as a first step for the theoretical understanding of complex exchange couplings of manganese spins in manganese-oxygen clusters. Table 2 summarizes the typical manganese clusters, observed effective exchange integrals and calculated θ values from Fig. 3. Theoretically proposed spin structures on the basis of the classical Heisenberg model [10, 28] are illustrated in Fig. 9.

4.3.1 Cyclic manganese oxide clusters

The binuclear manganese acetate complex (**5d**) with the Mn(II)OMn(II) core has a positive J_{12} value, and

Table 2. Structure and spin properties of manganese oxide clusters

No.	System	J	θ_{ij}	Alignments	Ref.
5d	$[Mn(III)_2O(O_2CMe)_2]L$	$J = 9$	$\theta = 0°$	axial	40
5e	$Mn(IV)_4O_6(bipy)_6\ (ClO_4)_4H_2O$	$J_1 = -88$, $J_2 = -134$	$\theta = -180°$	axial	41
13b	$[Mn(II)Mn(III)_2O(O_2CMe)_6(pyr)_3](pry)$	$J_1 = -8.3$, $J_2 = -5.1$	$\theta_{12} = \theta°, \theta_{13} = 180°$	axial	44
15a	$[Mn(III)O(O_2CMe)(pyr)_3]_3(ClO_4)_2$	$J_1 = J_2 = -10$	$\theta = 120°$	triangular	43
15b	$[Mn(IV)_3O_4(OH)(bpea)_3](ClO_4)_3$	$J_1 = -11$, $J_2 = -76$	$\theta = 94.15°$	helical	45
15c	$[Mn(IV)_3O_4(H_2O)_4(bpy)_4]^{4+}$	$J_1 = -49$, $J_2 = -91$	$\theta = 105.62°$	helical	45
16b	$[Mn(III)Mn(IV)O_2)_2(tphn)_2]^{4+}$	$J_1 = -101.1$, $J_2 = -8.4$	$\theta_{ij} = 90°$	axial	46
17b	$[Mn(II)\{Cu(II)(oxpn)_3\}](ClO_4)_2$	$J = -13.3$	$\theta_{ij} = 120°$	axial	47
18b	$[Mn(III)_4O_2(O_2CMe)_7(bipy)_2]^+$	$J_1 = -7.8$, $J_2 = -23.5$	$\theta_{13} = 99.6°$	helical	48
18c	$[Mn(II)_2Mn(III)_2O_2(O_2CMe)_6(bipy)_2]$	$J_1 = -1.97$, $J_2 = -3.12$	$\theta_{13} = 113.2°$	helical	51
32a	$[Mn(IV)\ Mn(III)_3(\mu\text{-}O)_3(\mu\text{-}Cl)]$	$J_1 = 11.3$, $J_2 = -13.1$	$\theta_{12} = 0°, \theta_{34} = \pi$	axial	61
33a	$[Mn(II)_4Te_4]$ (cubane)	$J = -21.7$	$\theta_{ij} = 109°$	T_d	54
33b	$[Mn(II)_4(\mu\text{-}OR)_4]$ (cubane)	$J_1 = -2.5 \sim 0.25$	$\theta_{ij} = 109°$ *or* $\theta_{12} = \theta_{34}$	T_d	52
35a	$[Mn(IV)_4O_6]^{4+}$ (adamantane)	$J = 6.9$	$\theta_{12} = \theta_{34} = 0°$	axial	53

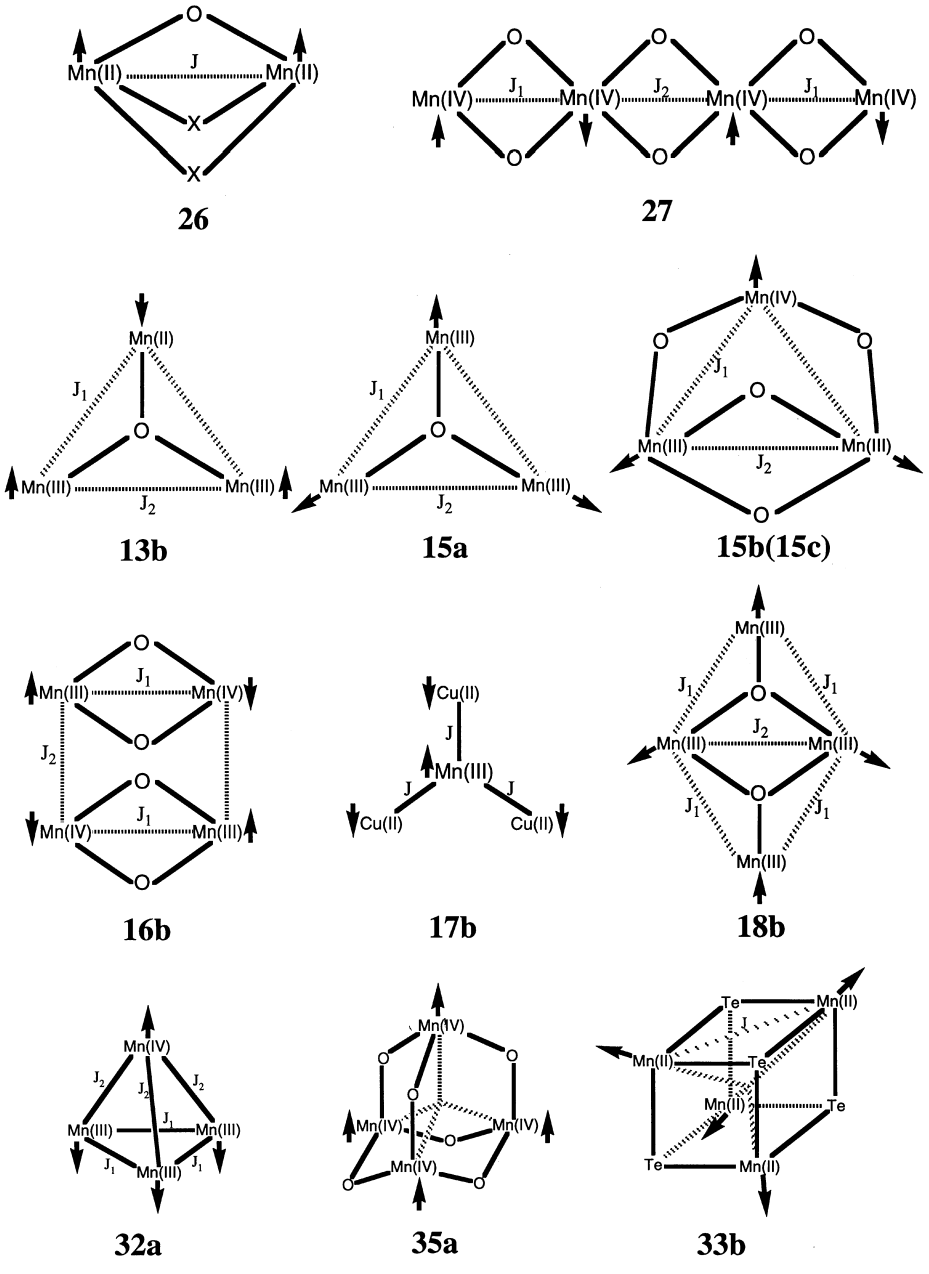

Fig. 9. Spin structures for manganese oxide clusters with linear triangular, cubane, adamantane and other structures

exhibits parallel spin alignment (**26**), where $S_{12} = S_1 + S_2 = 5$ [40]. On the other hand, the $[Mn(IV)(\mu_2 - O)_2]^{4+}$ cores exhibit strong antiferromagnetic exchange interactions ($J_{12} = -80$ to $-150\ cm^{-1}$). The Mn(IV) tetramer (**5e**) exhibits an axial spin structure (**27**) [41]. The Heisenberg model for Mn_3 systems with the C_{2v} symmetry in Fig. 2 is given by

$$\hat{H} = -J_1(S_T^2 - S_{12}^2) - J_2 S_{12}^2 \tag{14}$$

where $S_T = S_1 + S_2 + S_3$ is the total spin state, $J_{13} = J_{23} = J_1$ and $J_{12} = J_2$. From Eq. (14), the following conditions can be obtained for the cluster [42].

$$\sin\theta_{13} = 0 \tag{15}$$

$$\cos\theta_{13} = -S_3 J_1 / 2S_2 J_2 \quad (S_1 = S_2)\ , \tag{16}$$

where

$$\theta_{13} = -\theta_{23} \text{ or } \theta_{13} = l80 - \theta_{23}\ . \tag{17}$$

The conditions (15) and (16) give low-spin axial spin structures **13** and **14**. For example, Fig. 9 illustrates the axial spin structure (**13b**) for the $[Mn(III)_2Mn(II)O(O_2CMe)_6]$ core [43]. The total energies for **13** and **14** are independent of the easy axis of spins and are given by

$$E(\mathbf{13}) = -4S_1S_3J_1 + 2S_1S_2J_2 \tag{18}$$

$$E(\mathbf{14}) = -2S_1S_2J_2 \tag{19}$$

The more general (helical) solution (**15**) is derived from Eq. 16. The structure **15** in Fig. 7 is regarded as the triangular spin arrangement discussed previously [10, 20]. All the spin pairs in **15** exhibit singlet-type spin

coupling in contrast to the axial structures, for which one of the spin pairs is triplet-type. Therefore **15** plays a crucial role for a VB description of antiferromagnetic exchange couplings of spins in the cyclic maganese-oxygen clusters. The total energy for **15** is given by Eqs. (16) and (17) as

$$E(\mathbf{15}) = -S_3^2 J_1^2/J_2 - 2J_2 S_1 S_2 \tag{20}$$

The three Mn(III) ions in **15a** with the singlet ground state ($S_T = 0$) are magnetically equivalent; $S_1 = S_2 = S_3 = 2$ and $J_{12} = J_{23} = J_{31} = J$ [43]. Then all the angles for **15** are 120° in the D_{3h} form. **15** is more stable by SJ than the axial structures **13** and **14** at the geometry. This tendency holds even for the C_{2v} form under the following condition:

$$|S_3 J_1| < |2S_2 J_2| \ . \tag{21}$$

The condition is satisfied even in the case of a Jahn–Teller distorted cyclic Mn_3 system, but the reverse relation to Eq. (21) is expected for bent and linear Mn_3 systems, for which the axial structure **13** in Fig. 7 is found to be the ground spin structure. The condition (Eq. 21) is satisfied in the cases of the mixed valence (MV) Mn_3 complex **13b** [44]; it is noteworthy that the effective exchange integral involving the electron delocalization B, namely $J_{\text{eff}} = J_{ab} + B/S_a$, is used for the MV pair in the present model. The helical spin structures for **15** are completely characterized by three variables (S_{12}, S_3, S_T). The total spin state (S_T) is variable with the S_{12} value if S_3 is fixed. For example, the low-spin doublet ($S_T = 1/2$) state is given by **15**$(-1, 3/2, 1/2)$. Figure 10 illustrates the corresponding spin structures in the case of the $Mn(IV)_3$ ($S_3 = 3/2$) cluster.

Recent ESR experiments [45] have shown that the ground states of the Mn_3 complexes for **15b** and **15c** are quintet and doublet, respectively, and these are expressed by **15**(0, 3/2, 3/2) and **15**$(-1, 3/2, 1/2)$. By using the observed J_{ab} values, $\theta_{13}(-\theta_{23})$ and θ_{12} values are calculated to be 94° and 106°, respectively. The classical notations for **15b** and **15c** are compatible with the quantum vector models in Fig. 10.

The square planar $Mn(II)_2Mn(IV)_2$ complex (**16b**) with $S_T = 1$ [46] has an axial spin structure as shown in Fig. 9. The D_{3h} complex (**17b**) with $S_T = 1$ [47] also exhibits an axial structure like trimethylenemetane. The butterfly Mn_4 clusters are regarded as an edge-shared bi-triangle structure, where $J_{13} = J_{23} = J_{14} = J_{24} = J_1$, $J_{12} = J_2$ and $J_{34} = 0$. Then the Heisenberg Hamiltonian is given by

$$\hat{H} = -J_1(S_T^2 - S_{12}^2 - S_{34}^2) - J_2 S_{12}^2 \ , \tag{22}$$

where $S_T = S_{12} + S_{34}$ and $S_{34} = S_3 + S_4$. Possible lower spin structures are easily derived like the results for triangles as illustrated in Fig. 10. The butterfly complex **18b** with $S_T = 3$ [48] has a helical spin structure **9**$(-1, 4, 3)$. In fact, θ is calculated to be 100°, while it is 113.2° for the MV butterfly complex **18C** with $S_T = 1$, [48], namely **9**$(-3, 4, 1)$. Thus the quantum and classical representations are consistent, expressing the spin flustration state.

The cubane-type and adamantane-type Mn_4 complexes have four spin vectors as shown in Fig. 2. The Heisenberg Hamiltonian for them is therefore given by

$$H = -2\Sigma J_{pq} S_p S_q \cos\theta_{pq} \quad (p, q = 1, 2, 3, 4) \ , \tag{23}$$

where

$$\cos\theta_{pq} = \cos\theta_{12/2}\cos\theta_{34/2} \quad (p = 1, 2; q = 3, 4) \ . \tag{24}$$

From Eqs. (23) and (24), the two different axial type arrangements **28** and **29** are obtained as illustrated in Fig. 11. Interestingly, the more complex solutions with 2D spin modulations are also feasible. Fig. 11 illustrates schematically their spin structures. **30** is regarded as one of the helical (screw) spin structures discussed by Yoshimori [49] and Nagamiya [50]. Furthermore, the cone-type spin structure **31** [10, 20] results as the most general spin alignment under the assumption that the magnitude of all the spins is equivalent.

$$\cos\theta_{pq} = -\cos^2\theta/2, \quad \theta = \theta_{12} = \theta_{34} \tag{25}$$

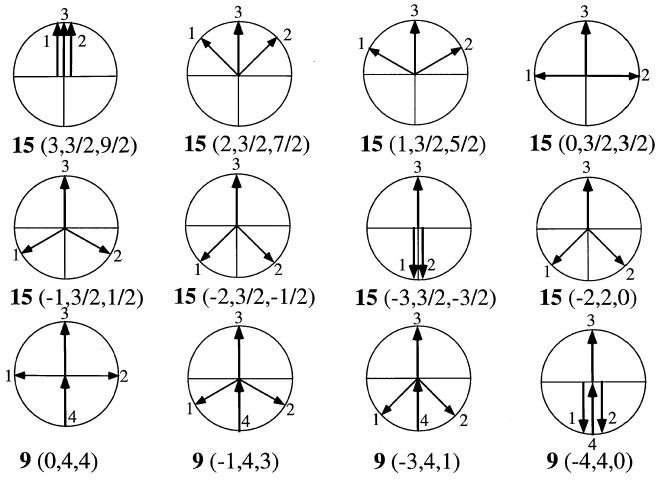

Fig. 10. Vector models (**15**) for three Mn(IV) ($S_a = 3/2$) systems with the quantum spin states (S_{12}, S_3, S_T), where S_{12} is given by the subtotal spin $(S_1 + S_2)$, and vector models (**9**) for the four Mn(III) ($S_a = 2$) systems with the quantum spin states (S_{12}, S_{34}, S_T)

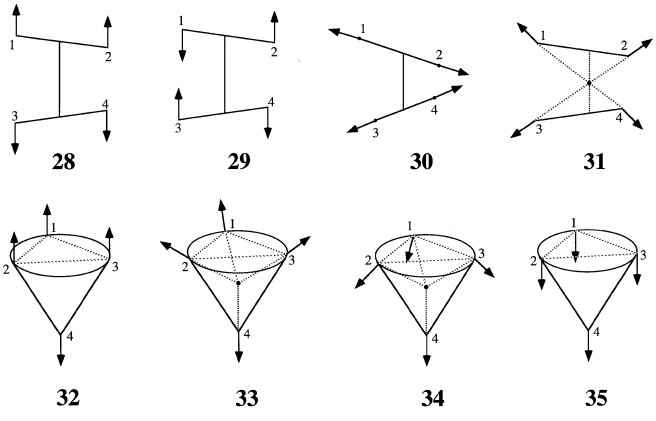

Fig. 11. Four different axial (**28**, **29**, **32**, **35**), helical (**30**), cone (**31**) and top (**33**, **34**) type spin alignments for four Mn_4 complexes, where oxygen anions are neglected

The total energies of axial and helical solutions were calculated on the basis of the exchange integrals (see Table 2) observed for the manganese pairs.

The top-type Mn_4 complex was also examined. The three Mn(III) ions are magnetically equivalent in this case. Then we can assume the following relations without loss of generality: $\theta_{12} = \theta_{23} = \theta_{31}$ and $\theta_{14} = \theta_{24} = \theta_{34}$, as illustrated in Fig. 2. The stationary conditions for Eq. (16) are easily obtained as

$$\sin\theta_{14} = 0 \tag{26}$$

$$\cos\theta_{14} = -J_1 S_4 / 3 J_2 S_1 \ , \tag{27}$$

where

$$\cos\theta_{12} = 1/2(3\cos\theta_{14} - 1) \tag{28}$$

The low-spin axial (**32**) and high-spin axial (**35**) solutions are similarly obtained from Eq. (26) as shown in Fig. 11. The MV cubane-type Mn_4 complex (**32a**) [51] and adamantane-like Mn_4 complex (**35a**) [52, 53] correspond to these cases, respectively. In addition to these axial solutions, the more general spin structures with a top-type structure, **33** and **34**, are possible for these species. The top-type structure was indeed feasible for the 4Fe-4S cluster; the optimized angles θ_{12} and θ_{14} are 119° and 102°, respectively, under the assumptions J[Fe(IV)-Fe(IV)] = −80 cm^{-1} and J[Fe(IV)-Fe(III)] = −60 cm^{-1}. The T_d spin structure is regarded as a special form of top or cone; $\theta_{ij} = 109°$. For example, the cubane-type Mn_4 complex (**33**) [54] has the negative J values satisfying this condition.

In conclusion, the spin vector model provides simple intuitive pictures for antiferromagnetic spin couplings between the high-spin manganese ions in MnO systems. The spin couplings are essentially determined by the balance of the magnitudes of the negative J_{ab} values for the nearest-neighbour iron pairs in the systems, leading to helical and general spin couplings [24, 25]. As shown previously [17], the antiferromagnetic spin structures are nothing but a VB representation of complex antiferromagnetic spin correlations in the clusters. This means that the magnetic moment itself becomes zero after spin rotation or spin projection, but the singlet-type spin correlation still exists after the space and time average. Recently many Mn_N oxide clusters (N = 7–12) have been synthesized [40]. Their spin structures are explained by combinations of axial, helical and more general spin structures for small clusters in Fig. 9. Interestingly, spin rotations are not free for these species because of strong anisotropy, which determines an easy axis of spin orientation.

5 Quantum dynamics of spins

5.1 Macroscopic quantum tunneling

Symmetry and broken symmetry become particularly important in the field of mesoscopic magnetic clusters with strong anisotropy, which are indeed intermediate between microscopic (quantum) and macroscopic (classical) particles. For example, MQT and/or MQC [9, 55] have been the subject of much interest because of the anisotropy barrier height. In fact, the manganese acetate complex, $Mn_{12}O_{12}(CH_3COOH)_{16}(H_2O)_4 = Mn_{12}$-Ac, exhibited several characteristics of MQC and MQT which were revealed by measurements of the ac magnetic susceptibility, relaxation time, M-H curve, etc. [56–60]. Therefore, a theoretical study of the complex is particularly important to understand the nature of MQT and MQC.

Judging from preceding results for the small Mn clusters, many spin alignments are conceivable for the ground state of Mn_{12}-Ac, which contains four Mn(IV) ions in the central distorted cubane surrounded by eight Mn(III) ions. The low-spin helical spin alignment with strong spin flustration and high-spin axial spin alignment are illustrated in Fig. 12. Magnetic susceptibility measurements [57] have revealed that the ground state of the typical Mn_{12}-Ac complex is high spin ($S = 10$), though other types of this complex have the $S = 9$ and $S = 9.5$ ground spin states [61]. The

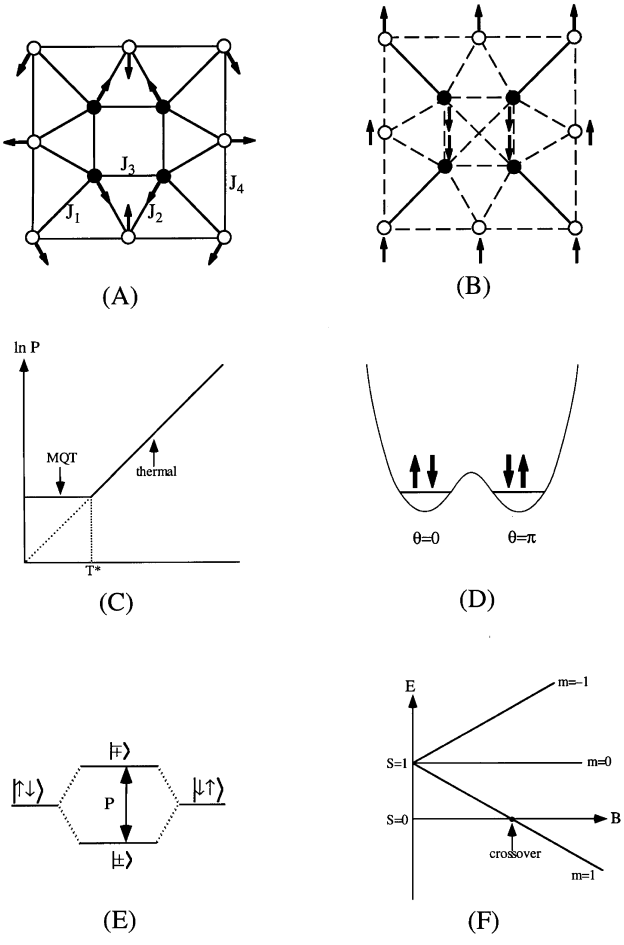

Fig. 12A–F. Diagrams for Mn_{12}-Ac. **A** and **B** illustrate helical and axial spin structures in Mn_{12}-Ac. **C** shows a typical dependence of the quantum tunneling rate on the temperature in relation to the macroscopic quantum tunneling and the crossover temperature (T^*). Double-well potential for the spin states and a spin state picture for the quantum tunneling rate are shown in **D** and **E**, respectively. **F** depicts the spin crossover induced by the external magnetic field

simulations of the magnetic data [57] using the Heisenberg model in Fig. 12 indicated three different ground states depending on J_2 and J_3 values under the assumption that $J_1 = -150$ and $J_4 = 0$ cm^{-1}; (a) $S = 8$ ($J_2 = -60$ and $J_3 = -60$), (b) $S = 0$ ($J_2 = -60$ and $J_3 = -62.5$) and (c) $S = 10$ ($J_2 = -60$ and $J_3 = -57.5$). The energy difference between the low-spin ($S = 0$) and the high-spin ($S = 10$) states is small. This result is not at all surprising since many spin flustrated structures shown in Figs. 9–11 are conceivable in the Mn_{12}-Ac complex.

The Mn_{12}-Ac complex can be treated as a single spin ($S = 10$) object because of its low temperature property [56–61]. Since the magnetic anisotropy is rather strong, the magnetic moment **M** aligns in parallel and antiparallel manner along the easy axis as illustrated in Fig. 13A. However, **M** can tunnel between the energy minima, providing the in (+) and out-of-phase (−) states in Fig. 13B, where P denotes the tunneling matrix element. The quantum average of the magnetic moment $\langle \mathbf{M} \rangle$ disappears in the resonating state, though $\langle \mathbf{M}^2 \rangle = S^2$ ($S =$ size of spin). The time correlation function $S(t)$ of **M** oscillates with neglect of dissipation because of the MQC effect [55]

$$S(t) = \langle \mathbf{M}(t)\mathbf{M}(t + \Delta t) \rangle = S^2 \cos 2P\Delta t \ . \tag{29}$$

The Fourier transform of $S(t)$ gives the $S(\omega)$ value ($= \delta(\omega - \omega_{\mathrm{res}})(h\omega_{\mathrm{res}} = 2P)$, which is related to the imaginary part $\chi''(\omega)$ of the frequency-dependent magnetic susceptibility through the fluctuation-dissipation theorem. In fact, several experiments have confirmed the frequency-dependent peaks of $\chi''(\omega)$ for polycrystalline samples of the Mn_{12}-Ac complex [56–61].

In the presence of an external magnetic field, the symmetry of the potential surface in Fig. 13A is broken, and MQT from a metastable state to another state becomes essential. Here, model III in Ref. [55] is modified

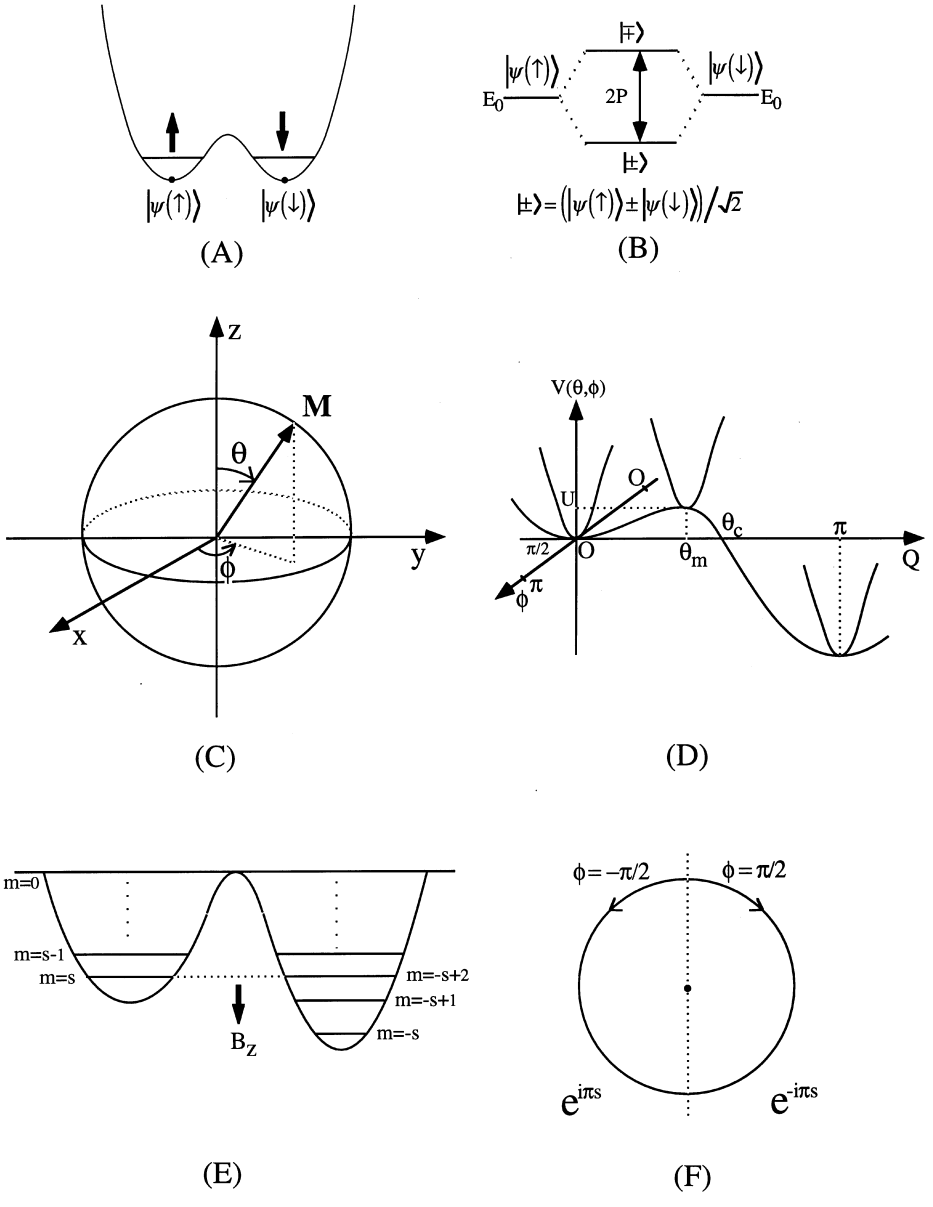

Fig. 13A–F. Double-well potential for the spin states and phase factor. **A** and **B** illustrate a double-well potential for the spin states in a mesoscopic system and the quantum tunneling rate in relation to the molecular orbital picture, respectively. A vector model for a magnetic moment and its total potential energy curve $V(\theta, \varphi)$ are shown in **C** and **D**, respectively. **E** depicts a unsymmetrical potential curve involving the effect of an external magnetic field. **F** illustrates a topological diagram for the phase factor

for our purpose. To this end, the anisotropy energy $E_{\rm anis}$ and the interaction energy $E_{\rm int}$ between the spin and the applied field B are expressed using the polar coordinates in Fig. 13C.

$$E_{\rm anis} = -\frac{K}{2}S^2\cos^2\theta + \frac{\lambda K}{2}S^2\sin^2\theta\cos^2\phi \tag{30}$$

$$E_{\rm int} = -\mu_{\rm B}BS\cos\theta \tag{31}$$

Figure 13D illustrates the profile of the total potential energy, $V(\theta,\phi) = E_{\rm anis} + E_{\rm int}$, which is approximately expressed by the 1D form assumpting strong anisotropy along the x-axis ($\lambda \gg 1$ and then $2\phi = \pi$). Therefore the resulting 1D potential $V(\theta,\pi/2) = V(\theta)$, is given by a single parameter as

$$V(\theta) = \frac{K}{2}S^2\left[\cos^2\theta + 2\frac{B}{B_{\rm c}}(\cos\theta - 1)\right] \tag{32a}$$

$$\cong \frac{K}{2}S^2\left[\varepsilon^2\theta - \frac{\varepsilon^4}{4}\right] \ , \tag{32b}$$

where the constant term is added so as to satisfy the condition $V(0) = 0$ as illustrated in Fig. 13D. $B_{\rm c}$ is the coercive field given by $KS/\mu_{\rm B}$.

In order to compute the tunneling rate P in Eq. (29), we consider the imaginary time transition amplitude expressed as a coherent state path integral for spins [25,27]

$$\langle\pi|{\rm e}^{-\beta H}|0\rangle = \int D\Omega{\rm e}^{-S_\theta} \ , \tag{33}$$

where $|\pi\rangle$ and $|0\rangle$ denote the coherent states responsible for up- and down-spin alignments. The Euclidean action S_θ is given by

$$S_\theta = \int d\tau\left[\frac{\theta^2}{K\lambda} + V(\theta)\right] \ . \tag{34}$$

The potential energy $V(\theta)$ in Eq. (32a) is usually expanded into a power series of θ in Eq. 32(b), assuming that $B = B_{\rm c}(1-\varepsilon)(\varepsilon \ll 1)$ to obtain the well-known analytical (bounce) solution

$$\theta = \theta_{\rm c}[\cosh\omega_0\tau]^{-1} \ , \tag{35}$$

where $\theta_{\rm c} = 2\sqrt{\varepsilon}$ and $\omega_0 = KS\sqrt{\lambda\varepsilon}$. In the bounce solution, θ varies from $\theta = 0$ at $\tau = -\infty$ to $\theta_{\rm c} = 0$ at $\tau = 0$, and then back to $\theta = 0$ at $\tau = \infty$. The action S_θ is also given by, $\frac{16U}{3\omega_0}$ where U is the classical activation barrier in Fig. 13D at $\theta_{\rm m} = \sqrt{2\varepsilon}$. Thus, we obtain the tunneling probability by the path integral method [25] as

$$P = \omega_0\exp(-S_\theta) = \omega_0\exp\left(-\frac{16U}{3\omega_0}\right) \ . \tag{36}$$

Since the thermal transition probability $P_{\rm th}$ is given by $\exp(-U/kT)$, the crossover temperature (T^*) from thermal activation to quantum tunneling is given by $3\omega_0/16k$. This crossover phenomena was indeed observed for the M_{12}-Ac complex as illustrated in Fig. 12C, where $T^* = 2K$ [60]. From Eq. (36), the frequency ω_0 should become high to obtain higher T^*, and therefore both the anisotropy constant K and the size of the spin S are required to increase by chemical modifications (see later).

In the above derivation, we did not consider the topological term, which appears in the Euclidean Lagrangian. Note that the action $S_{\theta,\phi} = \int d\tau L$ in general

$$L = -ihS\dot{\phi}(1-\cos\theta) + H(\theta,\phi) \ , \tag{37}$$

where the second term denotes the Hamiltonian for the spin system, which is assumed not to involve the external field; namely we consider the case in Fig. 13A, and then obtain the so-called instanton solution as an analytical solution [55]. The former term provides the phase factor, $\exp(\pm i\pi S)$ relating to the so-called winding number as illustrated in Fig. 13F, where ϕ is taken to be $\pm\pi/2$ [ϕ is replaced by θ in Eq. 30 (vice versa) to understand the pole] [62]. This phase factor gives the boundary contribution to $S_{\theta,\phi}$, and plays a crucial role in modifying the transition probability P as

$$P\ ({\rm tunnel}) = |\cos(\pi S)|P \ . \tag{38}$$

The phase factor $|\cos(\pi S)|$ represents an interference between the instanton and antiinstanton contributions to tunneling. If the spin is an integer, the interference is constructive, and the total tunneling rate is of the order P, but it is destructive for the half-integer spin, leading to zero tunneling rate.

The exact quantum treatment is feasible for magnetic clusters such as the Mn_{12}-Ac complex [60]. The simplest Hamiltonian is obtained from Eq. (32a) as

$$\hat{H} = -DS_z^2 - g\mu_{\rm B}S_zB_z \ , \tag{39}$$

where D is the uniaxial anisotropy energy constant which is expressed by K and λ in Eq. (30), and B_z is the applied magnetic field (see Eq. 31). There are 21 Zeeman sublevels ($2S+1 = 21$ and $10 \geq m \geq -10$) for the ground state of the Mn_{12}-Ac complex as shown in Fig. 13E. The two levels with S and $(-S+n)$ become degenerate in energy by changing the transverse field B_z as

$$-DS_z^2 - g\mu_{\rm B}S_zB_z = -D(n-S_z)^2 - g\mu_{\rm B}(n-S_z)B_z \ . \tag{40}$$

Then the resonance quantum tunneling between these two states occurs at the applied field B_z(resonance) $= -nD/g\mu_{\rm B}$; the phase factor in Eq. (38) should be also considered for these states. The observed quantum jump of the magnetization curve for the Mn_{12}-Ac complex by sweeping B_z can be explained by this tunneling mechanism since the size of spin changes abruptly from S^2 to $(S-n)^2$ [60].

Very recently, the ac susceptibility $\chi''(\omega)$ was observed for the Mn(IV)Mn(III)$_3$O$_3$Cl complex with the half-integer spin ($S = 9/2$)[63]. The slow relaxation of magnetization demonstrated a behavior of the single molecule magnet, but the hysteresis curve has not yet been recorded to allow Eq. 38 to be examined. Probably several experiments will be performed in the near future to confirm the topological rule, though it is suppressed by many relaxation effects. The experiments already showed that the peak temperatures of $\chi''(\omega)$ of the manganese complexes are well correlated with the potential energy barriers arising from the anisotropy [63].

A next step from the theoretical side is therefore the design of new compounds which may exhibit MQC and

MQT at high temperature. Since a large anisotropy constant D and a large spin S, and topological factors (integer or half-integer spin) are required for this purpose, transition metal and rare-earth metal carcogenides would be possible candidates. For example, clusters of clusters will be interesting as shown in Fig. 15 (see Sect. 6).

5.2 MQC for antiferromagnetic molecular magnets

We consider a simple model of two interacting spins of the same size S [64]. The Heisenberg Hamiltonian is given by

$$\begin{aligned}\hat{H} &= -\{D_1(S_1^z)^2 + D_2(S_2^z)^2\} - 2J\mathbf{S}_1 \cdot \mathbf{S}_2 \\ &= -D(\mathbf{S}_z)^2 - J(\mathbf{S}^2 - \mathbf{M}^2)/2 \cong -D(\mathbf{S}_z^2 - J\mathbf{S}^2)\ ,\end{aligned} \tag{41}$$

where $\mathbf{S} = \mathbf{M}_1 - \mathbf{M}_2$ and $\mathbf{M} = \mathbf{M}_1 + \mathbf{M}_2$. D and J are the anisotropy energy constant and effective exchange integral, respectively. Since the mutual orientation of $\mathbf{M}_1$ and $\mathbf{M}_2$ is opposite in the case of antiferromagnetic spin alignment, $\mathbf{M}$ is essentially zero. On the other hand, the Neel vector $\mathbf{S}$ is finite, and its direction given by θ is $|0\rangle = |\uparrow\downarrow\rangle$ and $|\pi\rangle = |\downarrow\uparrow\rangle$ in the local minimum of the potential curve as illustrated in Fig. 12D. However, the broken-symmetry configuration $|0\rangle$ can tunnel across the anisotropy barrier to the other configuration $|\pi\rangle$, and the broken symmetry is recovered like the spin projection. Then the situation is quite similar to the case of a ferromagnetic particle discussed earlier. The energy splitting P is not negligible because of this tunneling as shown in Fig. 12E. P is calculated by using the instanton model as shown in Eq. (36), and the Euclidean action S_θ is given by $C\sqrt{D/J}$ (C = const) [64]. Since $|J|$ is larger than D in many transition metal oxides, the P value for antiferromagnetic particles is usually larger than the ferromagnetic P value. Therefore, molecular magnets with antiferromagnetic exchange interactions are interesting from this point of view. This is the reason why we examined the antiferromagnetic couplers reported in Sect. 3.

5.3 Magnetic field induced spin transitions

The magnetic field induced transition from the ground singlet state to the lower-lying high-spin state is an interesting subject, particularly in the case of antiferromagnetic molecular magnets as illustrated in Fig. 12F. In fact, such transitions were observed for several transition metal complexes such as the Fe_{10} complex [65]. We have performed ab initio PIMC simulations using UNO for simple biradical systems [25, 27, 66] as a model of the Fe complex. The ab initio UNO PIMC method certainly indicated the sharp transition of magnetization, which was responsible for the singlet to triplet transition under an applied magnetic field.

We have considered single or two-spin systems for simplicity. However, more realistic spin Hamiltonians constructed of each spin at the transition metal ions are necessary to investigate magnetic behavior at high temperature.

$$\begin{aligned}\hat{H} = &-\sum_{a,b} 2J_{ab}S_a^zS_b^z - \sum_a D_a(S_a^z)^2 - \sum_a \Gamma_a S_a^{\pm} \\ &- g\mu_B \sum_a S_a^z B_z + H_{SB}\end{aligned} \tag{42}$$

where $a(b)$ denotes the site of the magnetic ion. The dissipation term H_{SB} expresses the couplings of spins with many other freedoms such as phonon, etc. For example, H_{SB} is given by the so-called spin-boson model as

$$\hat{H}_{SB} = -\sum_a \kappa_a(S_a^+ b + S_a^- b^+) + \mu b^+ b \tag{43}$$

where $b(b^+)$ denotes the boson [67]. The population and phase relaxation processes will be investigated by the quantum simulation methods developed recently. The model Hamiltonian can be regarded as an extended Jaynes–Cummings model [68], where the boson is regarded as a photon, $\mu = h\omega$. Several common interests exist in the fields of quantum dynamics of spins and quantum optics, which are not touched on in this article; a comprehensive review of our theoretical results relating to the latter topics is given in Ref. [69]. On the other hand, the localized spin interactions with fermionic baths constructed of conducting electrons are described by a generalized Kondo model [36], which has also become important because of recent synthetic efforts toward organic and organometallic Kondo systems [70].

6 Future prospects and concluding remarks

6.1 Symmetry breaking in the native cluster

The electronic structures of manganese oxides, iron oxides and iron-sulfur clusters in active sites of enzymes are often described by the broken-symmetry HF or density functional solutions [7, 42, 71–73]. Magnetic Mossbauer EPR and NMR spectroscopies have been applied to describe the magnetic properties and chemical bonds of these species. For example, some of the theoretical and experimental results for the iron-sulfur clusters [74–76] are summarized in Table 3. The UHF or spin-polarized DFT methods provide axial spin structure **13** for the 3Fe-4S cluster and structures **28** and **32** for the 4Fe-4S cluster. The more general HF (GHF) solutions are necessary for MO theoretical descriptions of helical-type (**15**), cone- or tetrahedral-type (**31**) and top-type (**33**) structures.

The 4Fe-4S cluster in native ferredoxin [75] is probably a typical example for explanation of symmetry breaking and spin flustration. The DFT calculation of the MV core $[Fe(2.5)_2Fe(3)S_4]^{3+}$ assuming the antiferromagnetic exchange coupling between the high-spin 2Fe-2S clusters, $[Fe(3)_2S_2]^{2+}$ ($S_{12} = 10/2$) and $[Fe(2.5)_2S_2]^{1+}$ ($S_{34} = 9/2$) was already reported [73]. This axial doublet structure (**28**) is compatible with the experimental result ($S_T = 1/2$) for the synthetic 4Fe-4S cluster [71]. However, the NMR experiments indicated that the MV fragment $[Fe(2.5)_2S_2]^{1+}$ should have a larger spin moment than the other fragment $[Fe(3)_2S_2]^{2+}$ in the case of the native 4Fe-4S cluster in ferredoxin [72].

The total doublet state should be described by $(S_{12}, S_{34}, S_T) = (8/2, -9/2, -1/2)$, $(6/2, -7/2, -1/2)$, or the linear combination of the two configurations; these are expressed by the cone-type (**31**) spin structure. Thus the native 4Fe-4S cluster has an unsymmetrical biological environment, which stabilizes this unique (broken-symmetry) chemical bond.

The removal of the Fe(2) component from $[Fe_4S_4]^{3+}$ cluster generates the 3Fe-4S cluster $[Fe(3)_3S_4]^{1+}$ with the triangular spin alignment (**15**) as illustrated in Fig. 14. Judging from the spin structures, this reaction should proceed smoothly without an abrupt change of antiferromagnetic spin couplings. The reductions of $[Fe(3)_3S_4]^{1+}$ to $[Fe(3)_3S_4]^{0}$ and $[Fe(3)_3S_4]^{1-}$ provide the axial structures **13** ($S_T = 2$) and **13** ($S_T = 5/2$), respectively. On the other hand, the electron capture of the oxidized 4Fe-4S cluster gives the MV cluster $[Fe(2.5)_4S_4]^{2+}$, which is expressed by the T_d spin structure (**31**) as illustrated in Fig. 14. This implies that the antiferromagnetic spin coupling in the oxidized form does not change drastically upon one-electron reduction. Such smooth change of the chemical bonding may be

Table 3. Structure oxidation state and spin properties of iron-sulfur clusters

System	Spin coupling	MO	Spin structure	Experiment
$[Fe(3)_3S_4]^{1+}$	**13** (10/2, −5/2,5/2)	UHF(DFT)	axial	
(S_{12},S_3,S_T)	**15** (8/2, −5/2, 3/2)	GHF	helical	
	15 (6/2, −5/2, 1/2)	GHF	triangular	$S_T=1/2$
$[Fe(2.5)_2Fe(3)S_4]^{0}$	**13** (9/2, −5/2, 2)	UHF(DFT)	axial	$S_T=2$
(S_{12},S_3,S_T)	**15** (7/2, −5/2, 1)	GHF	helical	
$[Fe(2.5)_2Fe(3)S_4]^{1-}$	**13** (9/2, −4/2, 5/2)	UHF(DFT)	axial	$S_T=5/2$
(S_{12},S_3,S_T)	**15** (7/2, −4/2, 3/2)	GHF	helical	
$[Fe(3)_2Fe(2.5)_2S_4]^{3+}$	**28** (10/2, −9/2, 1/2)	UHF(DFT)	axial	
(S_{12},S_{34},S_T)	**31** (8/2, −9/2, −1/2)	GHF	cone	$S_T=1/2$
	31 (6/2, −7/2, −1/2)	GHF	cone	$S_T=1/2$
$[Fe(2.5)_3Fe(2.5)S_4]^{2+}$	**28** (9/2, −9/2, 0)	UHF(DFT)	axial	
(S_{12},S_{34},S_T)	**31** (7/2, −7/2, 0)	GHF	T_d	$S_T=0$
	31 (5/2, −5/2,0)	GHF	T_d	$S_T=0$
$[Fe(2)_3Fe(3)S_4]^{1+}$	**32** (12/2, −5/2, 7/2)	UHF(DFT)	axial	$S_T=7/2$
(S_{123},S_4,S_T)	**33** (10/2, −5/2, 5/2)	GHF	top	$S_T=5/2$
	33 (8/2, −5/2, 3/2)	GHF	top	$S_T=3/2$
	33(6/2, −5/2, 1/2)	GHF	top	$S_T=1/2$
$[Fe(2.5)_2Fe(2)S_4]^{+1}$	**28** (9/2, −8/2, 1/2)	UHF(DFT)	axial	$S_T=1/2$
(S_{12},S_{34},S_T)	**31** (7/2, −8/2, −1/2)	GHF	cone	$S_T=1/2$
	31 (9/2, −6/2, 3/2)	GHF	cone	$S_T=3/2$
$[Fe(2.5)_2Fe(3)Co(2)]^{2+}$	**28** (9/2, −8/2, 1/2)	UHF(DFT)	axial	$S_T=1/2$
$[Fe(2.5)_2Fe(2)C0(2)]^{1+}$	**28** (9/2, −7/2, 2/2)	UHF(DFT)	axial	$S_T=2/2$

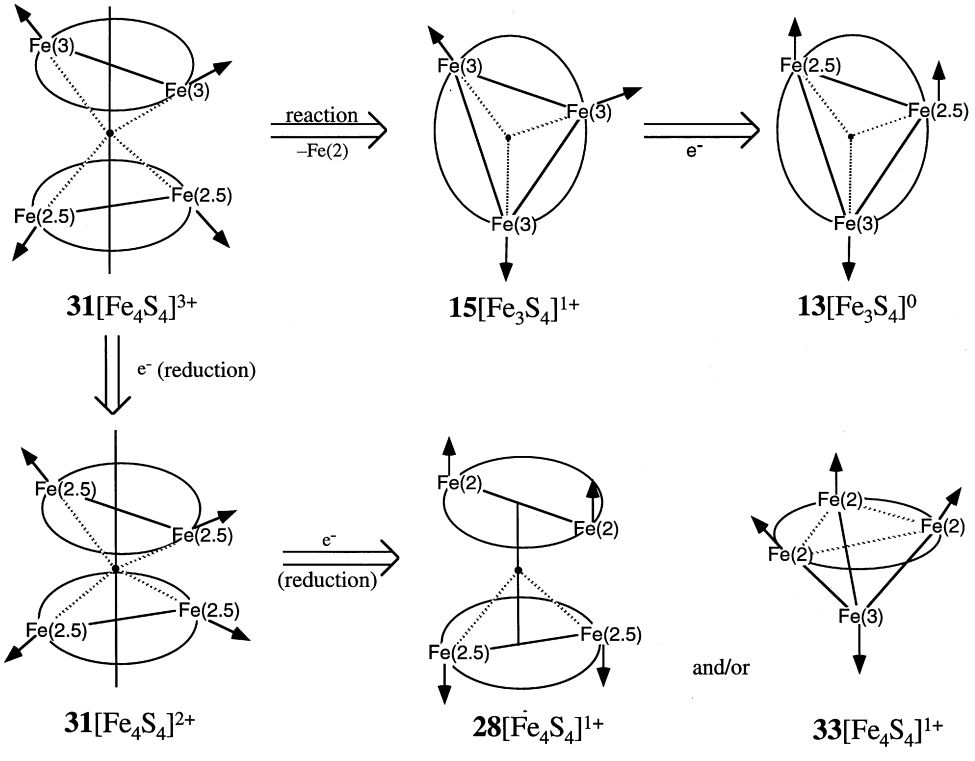

Fig. 14. Spin structures of the native 3Fe-4S and 4Fe-4S clusters in ferredoxins and variations of the structures with electron transfers

true for the reduction of $[Fe(2.5)_4S_4]^{2+}$ to $[Fe(2)_3Fe(3)S_4]^{1+}$, which is expressed by the top-type spin structure (**33**). The axial- (**28**) and cone-type (**31**) structures are also conceivable for the reduced cluster $[Fe(2.5)_2Fe(2)_2S_4]^{1+}$ if the MV fragment $[Fe(2.5)_2S_2]^{1+}$ is formed by electron capture. Several ground states with $S_T = 1/2$, 3/2, 5/2 and 7/2 were identified experimentally for the $[Fe_4S_4]^{1+}$ core, depending on the molecular structures and environmental effects in the native ferredoxins. The metal-substituted cores $[Fe(2.5)_{2.5}Fe(p)MS_4]$ ($p = 2$ or 3; M = Co^{2+}, Mo^{3+}, etc) have the axial structures (**28**) as shown in Table 3.

The above examples clearly show that magnetism and chemical bonds in the active sites of native ferredoxins can be regulated by the oxidation numbers and subtle changes of environment. This in turn allows active control of electronic structures by relatively weak interactions with external fields such as hydrogen bonding. We feel that such softness arising from the instability of the chemical bonds is a characteristic of these species and other active sites; for example the manganese oxide clusters in the water-oxidation site of the photosynthesis II system [71] and iron oxides in several oxygenation enzymes [4]. Our results indicate that MO theoretical models permitting 3D broken symmetries in Fig. 2 are inevitable even for qualitative descriptions of such labile chemical bonds.

6.2 Models of quantum wire and ring of spins

The three-centered units in Fig. 4 can be used as building blocks for molecular magnetic materials. Many kinds of radical centers are conceivable in **1**. Here we have examined the linear magnetic chains of the methyl radical with sulfur and oxygen couplers, which have antiferromagnetic exchange interactions. Judging from the negative sign of the J_{ab} values, many other antiferromagnetic chains are feasible as illustrated in Fig. 15. These species are regarded as the quantum wire of spins from the viewpoint of the magnetic field induced spin transitions. The quantum rings of spins are similarly constructed of these units to avoid the edge effects. The anisotropy effects for these organic clusters are very weak. Then these are regarded as pure antiferromagnetic Heisenberg systems, which are interesting regarding the Haldane problem [77,78].

On the other hand, transition metal ions and rare-earth metals can also be used as spin sources in the wire and rings, which exhibit strong anisotropy effects like the Mn_{12}-Ac complex. For example, the Mn clusters in Fig. 9 can be used as potential building blocks of clusters of clusters with large S and D as illustrated in Fig. 15. We have tried to synthesize a linear chain (about 13 units) of 4Fe-4S clusters using the metaphenylene bissulfide unit, but it was not isolated to characterize the magnetic property. The development of appropriate synthetic methods will probably be necessary for the synthesis of well-defined giant clusters. Many interesting phenomena should be found in such mesoscopic systems which exist in the crossover region between quantum and classical mechanics.

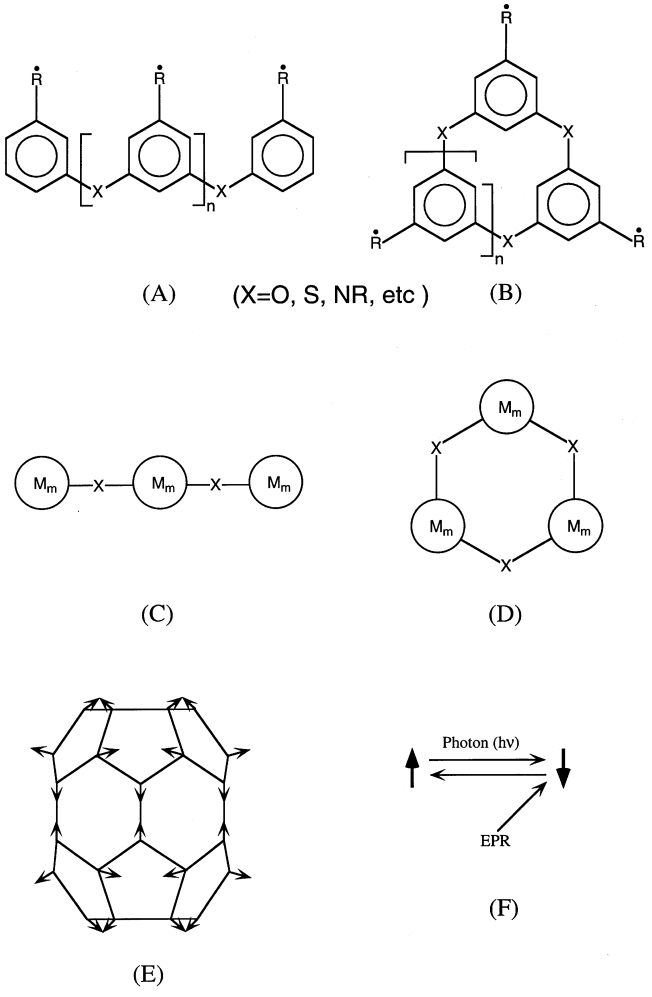

Fig. 15. Molecular design of linear (**A, C**) and ring (**B, D**) olygomers composed of organic and inorganic units, and possible spin structure for C_{36} **E**. **F** denotes the spin flip by the photon mode and the detection of it by EPR for quantum computing

6.3 Superconductivity via electron and spin correlations

In the past decade magnetism and electron correlation have attracted much interest in relation to high-temperature superconductivity in copper oxide. Many experimental and theoretical efforts have been made to elucidate the possible interplay between p and d electrons of transition metal oxides in an intermediate or strong electron-correlation regime [14, 36]. Over 10 years ago we presented ab initio molecular orbital calculations of effective exchange integrals in the Heisenberg model for transition metal oxo compounds [4]. It was shown that the magnitude of J_{ab} for the copper oxide unit is abnormally large compared with other transition metal oxo units in Fig. 4. After the discovery of high-temperature superconductivity for doped copper oxide, we immediately applied the calculated J_{ab} values to the estimation of the critical temperature T_c assuming a spin fluctuation model: $T_c = CJ_{ab}$ [34]. C is a constant whose explicit expressions are dependent on the theoretical models employed. Our theoretical hypothesis is

that a big J_{ab} may play an important role in possible spin-mediated superconductivity [34, 36].

During the past decade, we have been interested in the design and investigation of possible organic and organometallic analogs to copper oxides from the viewpoint of spin-mediated superconductivity. Since the spin flustration is remarkable in the fullerene compounds with C_5 units in Fig. 8, we may expect high-temperature T_c superconductivity for specific fullerene systems with strong spin flustration, though phonon freedom plays an important role in the case of superconductivity of C_{60} alkali systems. Very recently, C_{36} with D_{6h} symmetry was discovered as shown in Fig. 15E. The belt composed of the six-membered rings is antiaromatic, indicating that C_{36} would accept two electrons, becoming aromatic. The excess electrons coupled with spin flustration of the C_5 units may exhibit high-temperature superconductivity via the electron correlation mechanism, where both charge and spin fluctuations are important [14,36]. The nonalternant hydrocarbon units in Fig. 8 are interesting as building blocks for large spin flustration systems.

6.4 Molecular magnetic device

Recently many theoretical and experimental studies have been carried out for new models of computation; DNA, quantum and reversible computers. Single-molecule magnets such as the Mn_{12}-Ac complex [56–60] have received much interest in relation to a quantum computer, which utilizes the entanglement and superposition principle in quantum mechanics for parallel computation. Feynmann [79] first pointed out effects of the quantum mechanical phenomena on computation. He argued why this behavior might make it intrinsically computationally expensive to simulate quantum mechanics on a classical computer. By using quantum mechanics in computing, we compute more efficiently than with a classical computer. Beninoff [80] showed that a Turing machine could be simulated by the unitary evolution of a quantum process, which is a necessary prerequisite for quantum computation. Deutsch [81, 82] gave an explicit model of quantum computation. He defined both quantum Turing machines and quantum circuits and investigated some of their properties. Landauer and Bennett [83, 84] investigated what effect arises from the miniaturization of computational circuits. When the circuit is miniaturized, it is found that the character is governed by quantum theory.

Quantum mechanical computing was already carried out by using NMR quantum computing, since the decoherence effect was not serious in the nuclear spin systems [85]. We similarly expect that quantum computing in terms of various single molecular magnets by controling the spins with the external magnetic field [86] or with the photon modes [87, 88] (see Fig. 15F) will be performed in the future, since EPR can read the output information. However, there are several problems such as quantum relaxations, decoherence, etc, to be overcome to realize the application of singl-molecule magnets in a molecular device for a quantum computer. Apparently much experimental and theoretical effort is necessary to overcome such problems. This in turn promotes deep understanding of mesoscopic systems. The quantum simulations of the magnetic field induced spin transitions [66] and nonlinear optical responses [69] of molecular materials are our first step [66] toward a goal. In conclusion, concepts of the symmetry and broken symmetry in space-spin variables play important roles for theoretical understanding and rationalization of several interesting phenomena, which are realized in mesoscopic molecular materials in the intersection area between quantum and classical mechanics.

Acknowledgements. One of the authors (K.Y) thanks the late Professor Fukui for his continuous encouragement of our theoretical study on molecular materials. This work was supported by Grants-in-Aid for Scientific Research on Priority Areas (No. 10132241, No. 10149101 and No. 1146102) from the Ministry of Education, Science, Sports and Culture, Government of Japan.

References

1. Yamaguchi K (1983) J Mol Structure (Theochem) 103:101
2. Yamaguchi K, Fukutome H, Fueno T (1973) Chem Phys Lett 22:461
3. Yoshioka Y, Yamaki D, Maruta G, Tsunesada T, Takada K, Noro T, Yamaguchi K (1996) Bull Chem Soc Jpn 69:3395
4. Yamaguchi K, Takahara Y, Fueno T (1986) In: Smith VH Jr, Schaefer HF III, Morokuma K (eds) Applied quantum Chemistry Reidel, Dordrecht, p155
5. Okamura T-A, Takano Y, Yoshioka Y, Ueyama N, Nakamura A, Yamaguchi K (1998) J Organomet Chem 569:177
6. Nishino M, Yamanaka S, Yoshioka Y, Yamaguchi K (1997) J Phys Chem A 101:705
7. Yoshioka Y, Kubo S, Yamaguchi K, Saito I (1998) Chem Phys Lett 294:459
8. Yamaguchi K, Fueno T (1986) Kagaku 41:585 (in Japanese)
9. Awshalom DD, DiVincenzo DP, Smith JF (1992) Science, 258:414
10. Yamaguchi K (1975) Chem Phys Lett 30:288
11. Yamaguchi K (1978) Chem Phys 29:117
12. Yamaguchi K, Toyoda Y, Fueno T (1987) Synth Met 19:81
13. Okumura M, Yamaguchi K, Nakano M, Mori W (1993) Chem Phys Lett 207: 1
14. Nagao H, Mitani M, Nishino M, Yoshioka Y, Yamaguchi K (1997) Int J Quantum Chem 65:947
15. Yamaguchi K, Yoshioka Y, Fueno T (1976) Chem Phys Lett 46:360
16. Yoshioka Y, Yamaguchi K, Fueno T (1978) Theor Chim Acta 45:1
17. Bradley CJ, Cracknell AP (1972) The mathematical theory of symmetry in solids. Clarendon Press, Oxford
18. Fukutome H (1974) Prog Theor Phys 52:115
19. Yamaguchi K, Yoshioka Y, Takatsuka T, Fueno T (1978) Theor Chim Acta 48:185
20. Yamaguchi K, Fueno T, Ozaki M-A, Ueyama N, Nakamura A (1990) Chem Phys Lett 168:56
21. Yoshioka Y, Kubo S, Kiribayashi S, Takano Y, Yamaguchi K (1998) Bull Chem Soc Jpn 71:573
22. Ozaki M-A (1985) J Math Phys 26:1514
23. Yamaguchi K (1980) Int J Quantum Chem Symp 14:269
24. Yamanaka S, Okumura M, Nakano M, Yamaguchi K (1994) J Mol Struct (Theochem) 310:205
25. Nagao H, Shigeta Y, Kawabe H, Kawakami T, Nishikawa K, Yamaguchi K (1997) J Chem Phys 107:6283
26. Yamanaka S, Okumura M, Yamaguchi K, Hirao K (1994) Chem Phys Lett 225:213

27. Nagao H, Ohta K, Nakano M, Yamaguchi K (1997) Int J Quantum Chem 65: 697
28. Yamaguchi K, Yoshioka Y, Fueno T (1977) Chem Phys 20:171
29. Yamaguchi K, Okumura M, Mori W, Maki J, Takada K, Noto T, Tanaka K (1993) Chem Phys Lett 210:201
30. Yamanaka S, Kawakami T, Nagao H, Yamaguchi K (1994) Chem Phys Lett 231:25
31. Yamaguchi K, Tsunekawa T, Toyoda Y, Fueno T (1988) Chem Phys Lett 143:371
32. Tatewaki H, Huzinaga S (1980) J Chem Phys 72:4339
33. Bednorz G, Muller KA (1986) Z Phys B 64:189
34. Yamaguchi K, Takahara Y, Fueno T, Nasu K (1987) Jpn J Appl Phys 26: L1362
35. Fujiwara M, Nishino M, Takamizawa S, Mori W, Yamaguchi K (1996) Mol Cryst Liq Cryst 286:185
36. Yamaguchi K, Int J Quantum Chem 37:167 (1990)
37. Kawakami T, Yamanaka S, Takano Y, Yoshioka Y, Yamaguchi K (1998) Bull Chem Soc Jpn 71:2097
38. Schlegel HB (1986) J Chem Phys 84:4530
39. Yamaguchi K, Hayashi S, Okumura M, Nakano M, Mori W (1994) Chem Phys Lett 226:372
40. Vincent JB, Christou G (1989) Adv Inorg Chem 33:197
41. Philouge C, Blondin G, Girerd J-J, Guilhem J, Pascard C, Lexa D (1994) J Am Chem Soc 116:8557
42. Yamaguchi K, Fueno T, Ueyama N, Nakamura A, Ozaki M (1989) Chem Phys Lett 164:210
43. Baikie ARE, Hursthouse MB, New DB, Thornston P (1978) J Chem Soc , Chem Commun 62
44. Libby E, McCusker JK, Schmitt EA, Folting K, Hendrickson DN, Christou G (1991) Inorg Chem 30:3486
45. Pal S, Chan MK, Armstrong WH (1992) J Am Chem Soc 114:6398
46. Kirk ML, Chan MK, Armstrong WH, Solomon EI (1992) J Am Chem Soc 114: 10432
47. Lloret F, Journaux J, Julve M (1990) Inorg Chem 29:3967
48. Vincent JB, Christou C, Chang H-R, Li Q, Boyd PDW, Huffmann JC, Hendrickson DN, Christou G (1989) J Am Chem Soc 111:2086
49. Yoshimori A (1957) J Phys Soc Jpn 14:807
50. Nagamiya T (1968) Solid State Phys 20:305
51. Wemple MW, Tsai H-L, Folting K, Hendrickson DN, Christou G (1993) Inorg Chem 32:2025
52. Aussoleil JA, Cassoux P, de Loth P, Tuchaguess J-P (1989) Inorg Chem 28:3051
53. Hagen KS, Westmoreland TD, Scott MJ, Armstrong WH (1989) J Am Chem Soc 111:1907
54. Stephan H-O, Chen C, Hendel G, Griesar K, Haase W (1993) J Chem Soc Chem Commun 886
55. Chudnovsky EM, Gunther L (1988) Phys Rev Lett 60:661
56. Caneschi A, Gatteschi D, Sessoli R, Barra AL, Brunel LC, Guillot M (1991) J Am Chem Soc 113:5873
57. Sessoli R, Tsai H-L, Schake AR, Wang S, Vincent JB, Folting K, Gatteschi D, Christou G, Hendrickson DN (1993) J Am Chem Soc 115:1804
58. Sessoli R, Gatteschi D, Caneschi A, Novak MA (1993) Nature (Lond) 365:141
59. Paulsen C, Park J-G, Barbara B, Sessoli R, Caneschi A, (1995) J Magn Magn Mater 140–144:1891
60. Thomas L, Lionti F, Ballou R, Gatteschi D, Sessoli R, Barbara B (1996) Nature (Lond) 383:145
61. Vincent JB, Tsai H-L, Blackman AG, Wang S, Boyd PDW, Folting K, Huffman JC, Lobkovsky EB, Hendrickson DN, Christou G (1993) J Am Chem Soc 115:12353
62. Loss D, DiVicenzo DP, Grinstein G (1992) Phys Rev Lett 69:3232
63. Aubin SMJ, Wemple MW, Adams DM, Tsai H-L, Christou G, Hendrickson DN (1996) J Am Chem Soc 118:7746
64. Krive IV, Zaslavskii OB (1990) J Phys Condens Matter 2:9457
65. Taft KL, Delfs CD, Papaefthymiou GC, Fener S, Gatteschi D, Lippard SJ (1994) J Am Chem Soc 116:823
66. Kawakami T, Nagao H, Ueda K, Mori W, Yamaguchi K (1996) Mol Cryst Liq Cryst 286:177
67. Leggett AJ, Chakravarty S, Dorsey AT, Fisher MPA, Garg A, Zwerger W (1987) Rev Mod Phys 59:1
68. Jaynes ET, Cummings F (1963) Proc Inst Elect Eng 51:89
69. Nakano M, Yamaguchi K (1997) Trends in Chem Phys 5:87
70. Yamaguchi K, Okumura M, Fueno T, Nakasuji K, Murata I (1991) Synth Met 41–43:3631
71. Blomberg MRA, Siegbahn PEM, Styring S, Babcock GT, Akermark B, Korall P (1997) J Am Chem Soc 119:8285
72. Schmitt E-A, Noodleman L, Barends EJ, Hendrickson DN (1992) J Am Chem Soc 114:6109
73. Dance IG, Fisher KJ (1994) Prog Inorg Chem 41:637
74. Holm RH (1992) Adv Inorg Chem 38:1
75. Bertini I, Turano P and Vila AJ (1993) Chem Rev 93:2833
76. Noodleman L, Case DA (1992) Adv Inorg Chem 38:423
77. Haldane FDM (1986) Phys Rev Lett 57:1488
78. Okumura M, Yamanaka S, Mori W, Yamaguchi K (1994) J Mol Structure(Theochem) 310:177
79. Feynman RP (1982) Int J Theor Phys 21:467
80. Beninoff P (1982) J Stat Phys , 29:515
81. Deutsch D (1985) Proc R Soc Lond Ser A 400:96
82. Deutsch D (1989) Proc R Soc Lond Ser A 425:73
83. Landauer R (1986) Foundations of Physics 16:551
84. Bennett C (1973) IBM J Res Dev 17:525
85. Gershenfeld NA, Chaung IL (1997) Science 275:350
86. Nagao H, Yamanaka S, Nishino M, Yoshioka Y, Yamaguchi K (1998) Chem Phys Lett (in press)
87. Nishino M, Yamaguchi K, Miyashita S (1998) Phys Rev B 58: 9303
88. Nagao H, Nakano M, Shigeta Y, Yamaguchi K (1998) J Microscopy (in press)